
Article:

Chen, L., Verhoosel, C.V. and de Borst, R. (2018) Discrete fracture analysis using locally refined T-splines. International Journal for Numerical Methods in Engineering, 116 (2). pp. 117-140. ISSN: 0029-5981

https://doi.org/10.1002/nme.5917

This is the peer reviewed version of the following article: Chen L, Verhoosel CV, de Borst R. Discrete fracture analysis using locally refined T-splines. Int J Numer Methods Eng. 2018;116:117–140, which has been published in final form at https://doi.org/10.1002/nme.5917. This article may be used for non-commercial purposes in accordance with Wiley Terms and Conditions for Self-Archiving.

INTERNATIONAL JOURNAL FOR NUMERICAL METHODS IN ENGINEERING
Int. J. Numer. Meth. Engng 2017; **00**:1–26

Discrete Fracture Analysis using Locally Refined T-splines

L. Chen[1], C.V. Verhoosel[2], R. de Borst[1]*

[1] *University of Sheffield, Department of Civil and Structural Engineering, Sheffield S1 3JD, UK*
[2] *Eindhoven University of Technology, Department of Mechanical Engineering, Eindhoven 5600 MB, The Netherlands*

SUMMARY

Locally Refined (LR) T-splines are used to model discrete crack propagation without a predefined interface. The crack is introduced by meshline insertions in the LR T-mesh, which yields discontinuous basis functions. To implement the method in existing finite element programs, Bézier extraction is employed. A detailed description is given how the crack path is inserted and how the domain is reparameterised after insertion. The versatility and accuracy of the approach to model discrete crack propagation without the crack path being predefined is demonstrated by two examples, namely an L-shaped beam and a Single Edge Notched beam. When the crack approaches the physical boundaries, limitations to reparameterisation arise, as will be discussed at the hand of a Double-Edge Notched specimen. Copyright © 2017 John Wiley & Sons, Ltd.

Received . . .

KEY WORDS: fracture; isogeometric analysis; LR T-splines; Bézier extraction; cohesive zone model

1. INTRODUCTION

The computational modelling of crack propagation is of crucial importance for understanding and predicting fracture. One of the major approaches for simulating fracture is the discrete crack model, in which it is tried to mimic the observation that fracture induces a topological change in the body. Starting from elementary analyses in which nodes of a finite element mesh were split in two when the stress had exceeded the tensile strength [1], a host of approaches have been developed within the framework of the finite element method. An important development was the introduction of remeshing, which enabled cracks to propagate in arbitrary directions, no longer restrained by the original lay-out of the finite element mesh, e.g. [2] who used linear elastic fracture mechanics, or [3, 4] for analyses that exploit the cohesive-zone model.

Another approach is the use of interface elements [5], which are very effective when failure occurs at an adhesive layer like in laminated composites [6–9], or when the crack path is known in advance [10–12]. Another way to use interface elements for fracture is to insert them a priori between all continuum elements [13]. Evidently, this leads to a significant computational overhead and to an increased, non-physical elastic compliance in the interfaces prior to cracking. A method that causes only minimal topological changes while simulating the crack in a discrete manner is the eXtended Finite Element Method, which exploits the partition-of-unity property of finite element shape functions [14–18].

More recently, isogeometric analysis (IGA) has also been employed for the analysis of discrete crack propagation [19–25]. Due to the smoothness of the spline basis functions which are used in isogeometric analysis, the stress field around the crack tip is improved compared to standard finite

---

*Correspondence to: R. de Borst, University of Sheffield, Department of Civil and Structural Engineering, Sheffield S1 3JD, UK. E-mail: r.deborst@sheffield.ac.uk element analyses, leading to a superior prediction of the onset and the direction of crack propagation. Similar to finite elements, interface elements can also be used in an isogeometric context, with indeed a more accurate stress field around the crack tip, but with the same restriction as standard finite elements with respect to the fact that they are restricted to adhesive crack propagation or when the crack path is known in advance [20–24]. Further, when the splines basis functions satisfy the partition-of-unity property, an enrichment in the sense of the eXtended Finite Element method can also be used within isogeometric analysis, thus allowing for the propagation of discrete cracks independent from the underlying discretisation [26].

The full potential of isogeometric analysis for discrete crack analysis becomes apparent when the possibility is exploited to increase or lower the order of the spline functions that are used as the basis functions for the interpolation. By repeating the knot value in the parameter space, the order of the interpolation can be decreased locally, until $\mathcal{C}^{-1}$, and a discontinuity results in the physical space. For adhesive interfaces, where the crack path is known, Non-Uniform Rational B-Splines (NURBS) suffice [19, 24]. However, for crack propagation along a path that is *not* predefined, more flexible spline technologies are needed, less rigid, so that the basis functions in two and three dimensions can be built without resorting to a tensor-product structure.

In [19] T-splines have been used for this purpose. T-splines were introduced in [27] and were subsequently cast in a Bézier extraction framework in [28]. The mathematical properties of T-splines, such as linear independence and the partition-of-unity property, have been investigated in [29–32]. Upon mesh refinement a rapid convergence was found in [19] towards the experimental result. Also, little bumps in the load-displacement curve obtained for the coarser mesh, quickly disappeared for finer meshes. However, since also at the near-final crack configuration it must be possible to create T-junctions for further crack propagation, care must be taken that the initial mesh lay-out enables this. This requires an a priori knowledge of the crack path. A more versatile and general approach is to exploit T-splines in combination with local adaptivity. Recently, local refinement of T-splines has been investigated in [33–38].

In this contribution, we will employ Locally Refined T-splines (LR T-splines) [39] to initiate and propagate a discontinuity. LR T-splines are a combination of T-splines and LR B-splines, where the latter are obtained by locally enriching the space of the basis functions by replacing coarse grid B-splines by fine grid B-splines [40–44]. LR T-splines are constructed by meshline insertions into an initial T-mesh. It breaks the tensor-product structure input for LR B-splines, while it refines the domain in the parameter space instead of the vertex-grid for T-splines. The discontinuity is introduced in the parameter domain and the technology is very suitable for crack propagation analysis.

Herein, we first give a concise summary of the governing equations for the bulk and for the discontinuity. The LR T-spline finite element formulation is reviewed in Section 3. The introduction of discrete cracks in the LR T-spline finite element formulation is given next, followed by a discussion of some implementation aspects in Section 5. The reparameterisation of a body after a crack insertion is discussed in Section 6, while Section 7 presents numerical examples. A discussion then follows regarding the limitations of the method.

2. GOVERNING EQUATIONS FOR THE BULK AND THE INTERFACE

A crack is represented as an interface Γ_c in the physical domain Ω, see Figure 1. In this contribution linear elastic material behaviour is assumed, and the strong form of the equilibrium equations reads:

$$\begin{cases} \nabla \cdot \boldsymbol{\sigma} = \mathbf{0} & \text{on} \quad \Omega \\ \mathbf{u} = \hat{\mathbf{u}} & \text{on} \quad \Gamma_u \\ \boldsymbol{\sigma} \cdot \mathbf{n} = \hat{\mathbf{t}} & \text{on} \quad \Gamma_t \\ \boldsymbol{\sigma} \cdot \mathbf{n} = \mathbf{t}_c & \text{on} \quad \Gamma_c \end{cases} \tag{1}$$

where $\mathbf{n}$ denotes the normal vector at the boundary, $\hat{\mathbf{u}}$ and $\hat{\mathbf{t}}$ represent prescribed displacements and tractions, respectively, and $\boldsymbol{\sigma}$ is the Cauchy stress tensor. Assuming small displacement gradients,

DOI: 10.1002/nme

the kinematic equations read:

$$\boldsymbol{\varepsilon} = \frac{1}{2}\left(\nabla \mathbf{u} + (\nabla \mathbf{u})^{\mathrm{T}}\right) \quad \text{in} \quad \Omega; \qquad [\![\mathbf{u}]\!] = \mathbf{u}^{+} - \mathbf{u}^{-} \quad \text{on} \quad \Gamma_c \tag{2}$$

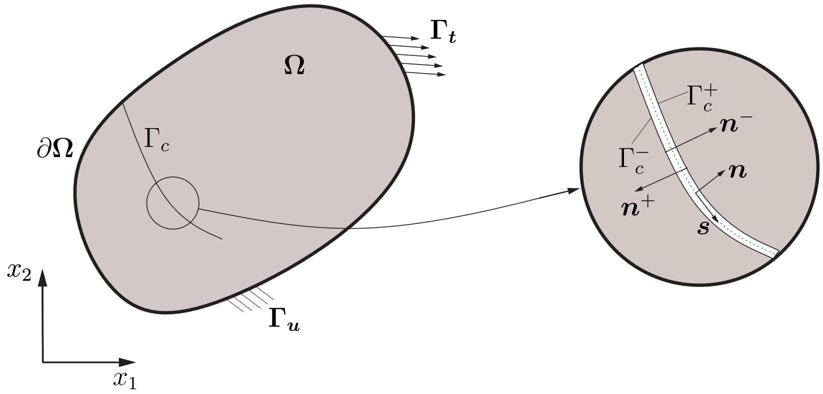

Figure 1. A solid body Ω with an internal discontinuity Γ_c. Γ_c is an interface boundary with positive and negative sides, Γ_c^+ and Γ_c^-, respectively.

In the bulk, Ω, the Cauchy stress tensor $\boldsymbol{\sigma}$ is assumed to be related to the strain tensor $\boldsymbol{\varepsilon}$ via the fourth-order elastic stiffness tensor $\mathbf{D}$ as:

$$\boldsymbol{\sigma} = \mathbf{D} : \boldsymbol{\varepsilon} \tag{3}$$

The crack opening $[\![\mathbf{u}]\!]$ is given in the global coordinate system (x_1, x_2) in the two-dimensional case considered in the remainder. The crack sliding and opening in the local coordinate system (s, n) (Figure 1) read:

$$[\![\boldsymbol{v}]\!] = \left([\![v_s]\!],\ [\![v_n]\!]\right)^{\mathrm{T}} = \mathbf{R}\,[\![\mathbf{u}]\!] = \mathbf{R}\left([\![u_{x_1}]\!],\ [\![u_{x_2}]\!]\right)^{\mathrm{T}} \tag{4}$$

with the rotation matrix $\mathbf{R}$. A traction – crack-opening relation links the traction on Γ_c to the displacement jump across it:

$$\mathbf{t}_c = \mathbf{t}_c\left([\![\boldsymbol{v}]\!]\right) = \{t_s,\, t_n\}^{\mathrm{T}} \tag{5}$$

The most important parameters in this cohesive-zone relation [45–47] are the fracture strength t_u, which is a measure for the maximum traction exerted on the interface Γ_c, and the fracture energy $\mathcal{G}_c$, which is the amount of energy that is needed to create a unit area of cracked surface. The shape of the decohesion curve can also significantly affect the fracture process [11]. The traction at the interface in the global coordinate system (x_1, x_2), $\mathbf{t}$, is obtained from the traction $\mathbf{t}_c$ via a standard transformation:

$$\mathbf{t} = \mathbf{R}^{\mathrm{T}}\mathbf{t}_c \tag{6}$$

It is finally noted that the cohesive-zone model includes the possibility of a traction-free crack, i.e. $\mathbf{t}_c = \mathbf{0}$, so that a linear-elastic fracture model can be considered as a limiting case. Of course, a stress singularity then arises at the crack tip, necessitating the use of special crack-tip elements.

3. ISOGEOMETRIC FINITE ELEMENT METHOD

The solution space, which is also used for the parameterisation of the geometry, should be constructed such that allows for: (i) an exact description of the domain geometry, and (ii) a discontinuous representation of the displacement field over Γ_c. To accomplish this, Locally Refined T-splines (LR T-splines) are employed, which can model pre-defined discontinuities as well as propagating discontinuities [39].

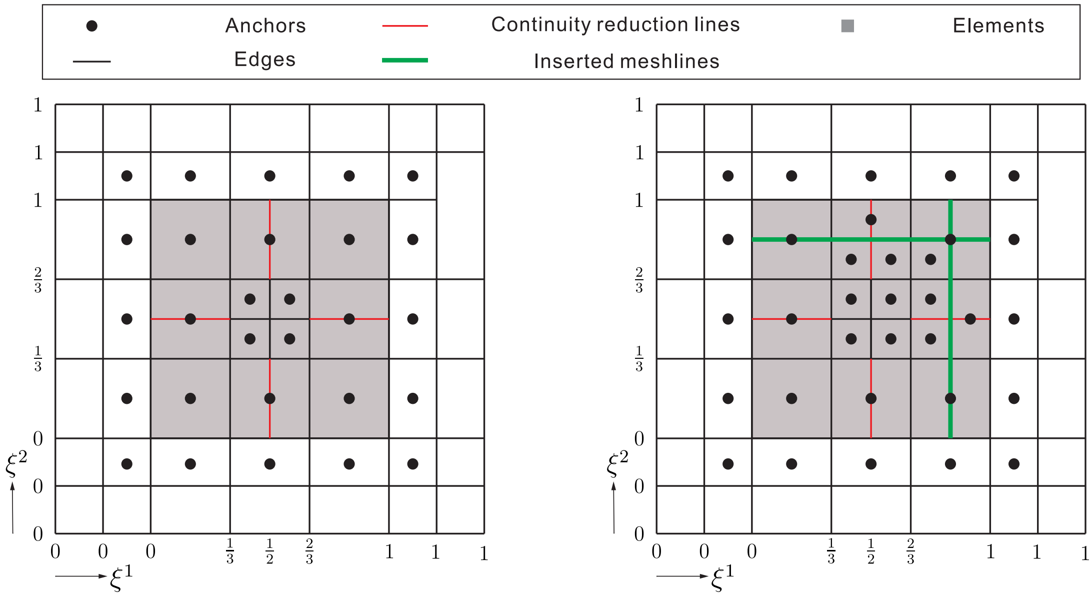

(a) initial T-mesh $\mathcal{T}_1$ (b) LR T-mesh $\mathcal{T}$

Figure 2. Example of an LR T-mesh in the parameter domain. The green lines indicate meshline insertions.

3.1. *LR T-spline fundamentals*

LR T-splines use a T-mesh as an input rather than a tensor-product mesh. We consider an initial T-mesh $\mathcal{T}_1$ with n anchors, which refer to locations of the blending functions in the parameter space. A local knot vector Ξ_i $(i = 1, \cdots, n)$ and a blending function $N_i\left(\xi^1, \xi^2\right)$ are prescribed for each anchor. If we insert a sequence of single meshlines $\{\varepsilon_i\}_{i=1}^{n}$ in $\mathcal{T}_1$, we obtain a nested Locally Refined T-mesh, $\mathcal{T}_n$, such that $\mathcal{T}_n \supset \mathcal{T}_{n-1} \supset \cdots \supset \mathcal{T}_2 \supset \mathcal{T}_1$, $\mathcal{T}_{i+1} = \{\mathcal{T}_i \cup \varepsilon_i\}$, see Figure 2. In an LR T-mesh, meshline insertions should (i) pass through an element (knot span), (ii) insert one meshline at a time, and (iii) span across $p + 2$ knots, or more. Here, p is the polynomial degree of blending functions. Elements are non-zero parametric areas confined by edges of a T-mesh, continuity reduction lines or inserted meshlines.

A meshline insertion ε on an LR T-mesh $\mathcal{T}_n$ is then either (i) a new meshline or an elongation of an existing meshline, or a continuity reduction line, or (ii) a joining of two existing meshlines or two existing continuity reduction lines, or (iii) an increase of the multiplicity of an existing meshline or continuity reduction line. For the case of an elongation, or a joining of existing meshlines or continuity reduction lines, we use their union to carry out the LR T-spline splitting.

The essence of LR T-splines is to maintain their minimal support property after meshline insertions in an LR T-mesh $\mathcal{T}$. That is, no other meshline traverses the interior space (support) of N. The refinement is realised by separate knot insertions in each parametric direction. We take the case of a knot insertion in the parametric direction ξ^1 as an example. An LR T-spline blending function N_i is defined by the local knot vectors

$$\Xi_i^1 = \left[\xi_1^1, \xi_2^1, \cdots, \xi_{i-1}^1, \qquad \xi_i^1, \cdots, \xi_{p+1}^1, \xi_{p+2}^1\right]$$

and

$$\Xi_i^2 = \left[\xi_1^2, \xi_2^2, \quad \cdots\cdots\cdots\cdots\cdots\cdots, \xi_{p+1}^2, \xi_{p+2}^2\right]$$

A new meshline, $\varepsilon = \hat{\xi} \times \left[\xi_1^2, \xi_{p+2}^2\right]$, is now inserted in $\mathcal{T}$, which leads to an insertion of $\hat{\xi}$ in Ξ_i^1 while keeping Ξ_i^2 constant. Two new local knot vectors, Ξ_{i1}^1 and Ξ_{i2}^1 are then obtained:

$$\begin{aligned} \Xi_{i1}^1 &= \left[\xi_1^1, \xi_2^1, \cdots, \xi_{i-1}^1, \hat{\xi}, \xi_i^1, \cdots, \xi_{p+1}^1 \qquad\quad\right] \\ \Xi_{i2}^1 &= \left[\qquad \xi_2^1, \cdots, \xi_{i-1}^1, \hat{\xi}, \xi_i^1, \cdots, \xi_{p+1}^1, \xi_{p+2}^1\right] \end{aligned} \tag{7}$$

DOI: 10.1002/nme

which yields two new anchors on $\mathcal{T}$ with respect to the local knot vectors Ξ^1_{i1} and Ξ^2_i, Ξ^1_{i2} and Ξ^2_i.

Applying this refinement procedure to all anchors on $\mathcal{T}$, we obtain updated anchors and updated elements on the refined LR T-mesh $\mathcal{T}_r$. Generally, meshline insertions reduce the continuity of T-spline blending functions. This is beneficial when inserting an interface $\Gamma_c\left(\xi^1,\ \xi^2\right)$ in a solid body Ω [19].

The LR T-spline blending functions are defined as

$$N_{\Xi}\left(\xi^1, \xi^2\right) = \gamma N_{\Xi^1}\left(\xi^1\right) N_{\Xi^2}\left(\xi^2\right) \tag{8}$$

with γ the scaling weight, which enables T-splines to satisfy the partition-of-unity property [39]. The set of LR T-spline basis functions is an LR T-spline basis $\mathcal{N} = \{N_i : \text{supp} N_i \in \mathcal{T}\}$. LR T-splines form a partition of unity and are nested, but are not necessarily globally or locally linear independent [39]. To enforce linear independence, several approaches have been proposed, including the hand-in-hand principle, the peeling algorithm and tensor expansion [39].

3.2. Control points update for the refined T-mesh

Blending functions are defined over the entire support (range of local knot vector) of an anchor. It is inconvenient to use the blending functions in a standard finite element data structure. However, Bézier extraction provides an elegant work-around by representing T-splines as element-wise Bernstein shape functions [28]. Consider an LR T-mesh $\mathcal{T}$ with E elements and n anchors. For anchor i, the local knot vectors are Ξ^1_i and Ξ^2_i, and the blending function N_i can be written as:

$$N^e_i\left(\xi^1, \xi^2\right) = [\mathbf{C}^e_i]^{\mathrm{T}} \mathbf{B}^e\left(\xi^1, \xi^2\right) \tag{9}$$

over element e with $(p+1)^2 \times 1$ Bernstein shape functions $\mathbf{B}^e\left(\xi^1, \xi^2\right)$ [31]. Here, we consider T-splines with an identical polynomial degree p in the ξ^1 and ξ^2 parametric directions. $\mathbf{C}^e_i$ is the Bézier extraction operator of anchor i over element e. Applying Bézier extraction to anchor i over E elements, we have a global Bézier extraction operator:

$$\mathbf{C}_i = \begin{bmatrix} \mathbf{C}^1_i \\ \vdots \\ \mathbf{C}^E_i \end{bmatrix} \tag{10}$$

Writing them for n anchors in a matrix form then leads to:

$$\mathbf{N}\left(\xi^1, \xi^2\right) = \mathbf{C}\mathbf{B}\left(\xi^1, \xi^2\right) = \begin{bmatrix} N_1\left(\xi^1, \xi^2\right) \\ \vdots \\ N_n\left(\xi^1, \xi^2\right) \end{bmatrix} = \begin{bmatrix} \mathbf{C}^{\mathrm{T}}_1 \\ \vdots \\ \mathbf{C}^{\mathrm{T}}_n \end{bmatrix} \begin{bmatrix} \mathbf{B}^1 \\ \vdots \\ \mathbf{B}^E \end{bmatrix} \tag{11}$$

We can apply Equation (11) to T-splines after meshline insertions. Consider an initial T-mesh $\mathcal{T}$ with n anchors. Inserting a series of single meshlines, $\{\varepsilon_i\}^n_{i=1}$, in $\mathcal{T}$ results in $\mathcal{T}_r$ with n_r anchors. T-splines $\mathcal{N}$ associated with $\mathcal{T}$ are now described by T-splines $\mathcal{N}_r$ associated with $\mathcal{T}_r$:

$$\boldsymbol{\Gamma}\mathbf{N}\left(\xi^1, \xi^2\right) = \boldsymbol{\Gamma}\mathbf{S}\mathbf{N}_r\left(\xi^1, \xi^2\right) \tag{12}$$

where $\mathbf{S}$ is the refinement operator [24, 39], $\mathbf{N}$ and $\mathbf{N}_r$ are the blending functions associated with $\mathcal{T}$ and $\mathcal{T}_r$, respectively, while $\boldsymbol{\Gamma}$ is a diagonal matrix with scaling weights γ of $\mathbf{N}$. Using Equation (11), we obtain:

$$\mathbf{N} = \mathbf{C}\mathbf{B}_r = \mathbf{S}\mathbf{C}_r\mathbf{B}_r \tag{13}$$

where $\mathbf{C}$ is the Bézier extraction operator of anchors on $\mathcal{T}$ over elements on $\mathcal{T}_r$, $\mathbf{C}_r$ denotes the Bézier extraction operator of anchors on $\mathcal{T}_r$ over elements on $\mathcal{T}_r$, and $\mathbf{B}_r$ contains Bernstein polynomials over elements on $\mathcal{T}_r$. The row values of $\mathbf{S}$ are obtained as:

$$\mathbf{C}_i = \mathbf{C}^{\mathrm{T}}_r \mathbf{S}_i \qquad \text{for} \qquad i = 1, \cdots, n \tag{14}$$

with the scaling weight γ^r of $\mathbf{N}_r$ obtained from Equation (12):

$$\boldsymbol{\Upsilon}^r = \boldsymbol{\Upsilon}\mathbf{S} \quad \text{with} \quad \boldsymbol{\Upsilon}^r = \left[\gamma_1^r,\, \gamma_2^r,\, \cdots,\, \gamma_{n_r}^r\right] \quad \text{and} \quad \boldsymbol{\Upsilon} = \left[\gamma_1,\, \gamma_2,\, \cdots,\, \gamma_n\right] \tag{15}$$

The control points associated with the T-mesh $\mathcal{T}_r$ are derived by the Bézier extraction operator [39]:

$$\mathbf{P}_r^w = \boldsymbol{\Gamma}_r^{-1}\mathbf{S}^{\mathrm{T}}\boldsymbol{\Gamma}\mathbf{P}^w \tag{16}$$

where $\boldsymbol{\Gamma}_r$ is a diagonal matrix with the scaling weight γ_β^r of $\mathbf{N}_r$ along the diagonal, see Equation (15). $\mathbf{P}^w$ and $\mathbf{P}_r^w$ are column vectors with control points $\mathbf{P}_\alpha^w$ and $\mathbf{P}_{r\beta}^w$, respectively. $\mathbf{P}_\alpha^w$ and $\mathbf{P}_{r\beta}^w$ are control points associated with $\mathcal{T}$ and $\mathcal{T}_r$, respectively, and $\mathbf{P}_\alpha = \left(x_\alpha^1,\, x_\alpha^2,\, w_\alpha\right)$ contains the coordinates of anchor α. The weighted coordinates of anchor α are $\mathbf{P}_\alpha^w = \left(w_\alpha x_\alpha^1,\, w_\alpha x_\alpha^2,\, w_\alpha\right)$.

3.3. Isogeometric finite element discretisation

In present study, the LR T-splines are employed to describe the solid geometry and to interpolate the displacement field $\mathbf{u}$ in an isoparametric sense:

$$\mathbf{x}\left(\xi^1, \xi^2\right) = \sum_{I=1}^{n_c} N_I\left(\xi^1, \xi^2\right)\mathbf{X}_I \qquad\qquad \mathbf{u}\left(\xi^1, \xi^2\right) = \sum_{I=1}^{n_c} N_I\left(\xi^1, \xi^2\right)\mathbf{U}_I \tag{17}$$

where $\mathbf{X}_I$ represents the coordinates of control points, $\mathbf{U}_I$ denotes the degrees of freedom at the control points, and n_c is the total number of control points. Writing Equation (1) in a weak form yields:

$$\int_\Omega \delta\boldsymbol{\varepsilon} : \boldsymbol{\sigma}\mathrm{d}\Omega + \int_{\Gamma_c} \delta\,[\![\mathbf{u}]\!]\cdot\mathbf{t}\left([\![\mathbf{u}]\!]\right)\mathrm{d}\Gamma = \int_{\Gamma_t} \delta\mathbf{u}\cdot\hat{\mathbf{t}}\mathrm{d}\Gamma \qquad \forall\delta\mathbf{u}\in\mathcal{V}_0 \tag{18}$$

where $\delta\varepsilon$, $\delta\mathbf{u}$ and $\delta\,[\![\mathbf{u}]\!]$ are admissible virtual fields. The solution $\mathbf{u}$ belongs to the function space $\mathcal{V}$:

$$\mathcal{V} = \left\{\boldsymbol{v} : v_i \in H^1(\Omega, \Gamma_c),\, v_i|\,\Gamma_D = \hat{u}_i\right\} \qquad\qquad \mathcal{V}_0 = \left\{\boldsymbol{v} : v_i \in H^1(\Omega, \Gamma_c),\, v_i|\,\Gamma_D = 0\right\} \tag{19}$$

in which H^1 denotes the first-order Sobolev space.

Considering Equations (2) and (17), the weak form Equation (18) gives:

$$\mathbf{f}_{\text{int}}\left(\mathbf{u}\right) = \mathbf{f}_{\text{ext}} \tag{20}$$

with

$$\mathbf{f}_{\text{int}}\left(\mathbf{u}\right) = \int_\Omega \mathbf{B}^{\mathrm{T}}\boldsymbol{\sigma}\mathrm{d}\Omega + \int_{\Gamma_c} \mathbf{H}^{\mathrm{T}}\mathbf{t}\mathrm{d}\Gamma \qquad\qquad \mathbf{f}_{\text{ext}} = \int_{\Gamma_t} \mathbf{N}^{\mathrm{T}}\hat{\mathbf{t}}\mathrm{d}\Gamma \tag{21}$$

Matrices $\mathbf{N}$, $\mathbf{B}$ and $\mathbf{H}$ contain shape functions, their derivatives, and relative displacements, respectively [19]. Linearisation gives the tangential stiffness matrix:

$$\mathbf{K}_{\tan} = \int_\Omega \mathbf{B}^{\mathrm{T}}\mathbf{D}\mathbf{B}\mathrm{d}\Omega + \int_{\Gamma_c} \mathbf{H}^{\mathrm{T}}\mathbf{R}^{\mathrm{T}}\mathbf{T}_c\mathbf{R}\mathbf{H}\mathrm{d}\Gamma \tag{22}$$

where $\mathbf{T}_c$ is the tangent stiffness of traction-opening law at the interface [20]:

$$\mathbf{T}_c = \frac{\partial\mathbf{t}_c}{\partial[\![\boldsymbol{v}]\!]} \tag{23}$$

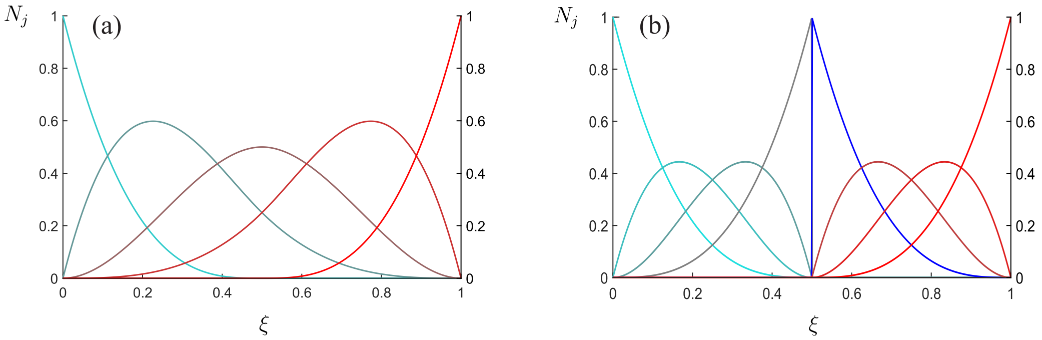

Figure 3. Cubic B-spline basis functions without (a) and with (b) discontinuity. The knot vectors for (a) are $\Xi = \{0, 0, 0, 0, 0.5, 1, 1, 1, 1\}$. For (b), the knot vectors read $\Xi = \{0, 0, 0, 0, 0.5, 0.5, 0.5, 0.5, 1, 1, 1, 1\}$.

4. DISCRETE CRACK REPRESENTATION IN ISOGEOMETRIC ANALYSIS

The non-zero knot intervals in Ξ^1 and Ξ^2 can be conceived as elements. If the knot value ξ_i^1 in Ξ^1 is repeated, the multiplicity of ξ_i^1 is denoted by m_i. Due to this multiplicity, the basis function N_{i,Ξ^1}^p becomes $\mathcal{C}^{p-m_i}$ continuous, which means that N_{i,Ξ^1}^p is $p - m_i$ times continuously differentiable over the knot i; see Figure 3. Due to this property, higher-order or lower-order continuity can be achieved. This can be employed to solve higher-oder differential equations, e.g. [48–54], but also to insert a discontinuity $\Gamma_c\left(\xi^1,\ \xi^2\right)$ in the model [19].

4.1. *Crack representation in the parameter domain*

In Figure 3b, the knot 0.5 is repeated $m = 3 + 1$ times. The basis functions are $\mathcal{C}^{-1}$-continuous at the knot 0.5. In Figure 4, the interface is defined along the parametric direction ξ^1 at $\xi^2 = \xi_d^2$. Meshline insertions (green lines in Figure 4a) are carried out to increase the multiplicity of ξ_d^2 to $m_d = p + 1$, which yields $\mathcal{C}^{-1}$-continuous basis functions.

In Figure 4, an LR T-mesh $\mathcal{T}$ is considered with multiplicities, which represents a discontinuous interface at $\xi^2 = 1/2$ in elements $e1$ and $e2$. Inserting such an interface requires $\mathcal{C}^{-1}$ continuous basis functions. These are constructed by using meshlines of multiplicity $m = p + 1$ [24]. In Figure 4(a), the number of meshlines at $\xi^2 = 1/2$ is $m = 2 + 1 = 3$. Due to this discontinuity, the coordinates of control points $1, \cdots, 4$ are equal to those of control points $5, \cdots, 8$, see Figure 4b. To shield this discontinuity from the rest of domain, we introduce $\mathcal{C}^0$ lines in the vertical direction at $\xi^1 = 1/3$ and at $\xi^1 = 2/3$, see Figure 4a. This enables a crack to propagate such that $\Gamma_c(t) \subseteq \Gamma_c(t + \delta t)$. To illustrate the discontinuity in Figure 4c, a shift $\left(\delta^1, \delta^2\right)$ has been applied artificially to control points $1, \cdots, 8$:

$$\begin{array}{lll} \left(\delta_1^1, \delta_1^2\right) = (-0.15, -0.15) & \left(\delta_2^1, \delta_2^2\right) = (-0.15, -0.15) & \left(\delta_3^1, \delta_3^2\right) = (-0.15, -0.15) \\ \left(\delta_4^1, \delta_4^2\right) = (-0.15, -0.15) & \left(\delta_5^1, \delta_5^2\right) = (0.15, 0.15) & \left(\delta_6^1, \delta_6^2\right) = (0.15, 0.15) \\ \left(\delta_7^1, \delta_7^2\right) = (0.15, 0.15) & \left(\delta_8^1, \delta_8^2\right) = (0.15, 0.15) & \end{array} \tag{24}$$

Figure 4c presents a crack passing through the element boundary at $\xi^2 = 1/2$. This crack not only separates elements $e1$ and $e2$, but also elements $e3$ and $e4$. In the analysis of crack propagation, the crack opening will be enforced only in elements $e1$ and $e2$, Figure 4d. This is achieved by applying constraints to control points $1, \cdots, 8$:

$$\begin{array}{lll} \left(\delta_1^1, \delta_1^2\right) = \left(\delta_5^1, \delta_5^2\right) = (0, 0) & \left(\delta_2^1, \delta_2^2\right) = (-0.15, -0.15) & \left(\delta_3^1, \delta_3^2\right) = (-0.15, -0.15) \\ \left(\delta_4^1, \delta_4^2\right) = \left(\delta_8^1, \delta_8^2\right) = (0, 0) & \left(\delta_6^1, \delta_6^2\right) = (0.15, 0.15) & \left(\delta_7^1, \delta_7^2\right) = (0.15, 0.15) \end{array} \tag{25}$$

In Figure 4d, the control points 1, 4, 5 and 8 are not at the crack tip. To determine the crack path after the crack nucleation and propagation, we need to parameterise the crack path after crack

DOI: 10.1002/nme

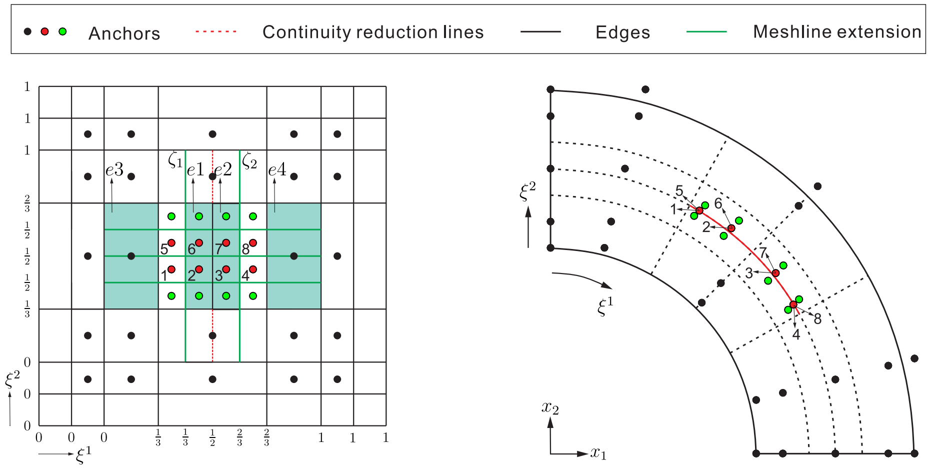

(a) Ω in the parameter domain (b) Ω in the physical domain

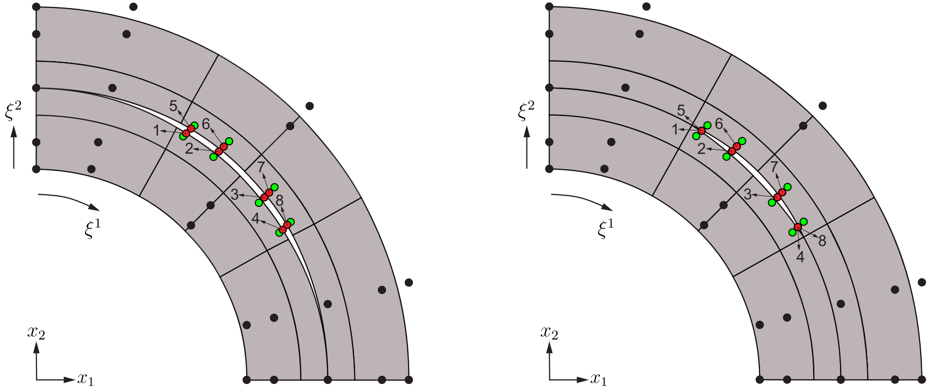

(c) Ω in the physical domain (d) Ω in the physical domain

Figure 4. Example of inserting an internal discontinuity Γ_c within a solid body Ω.

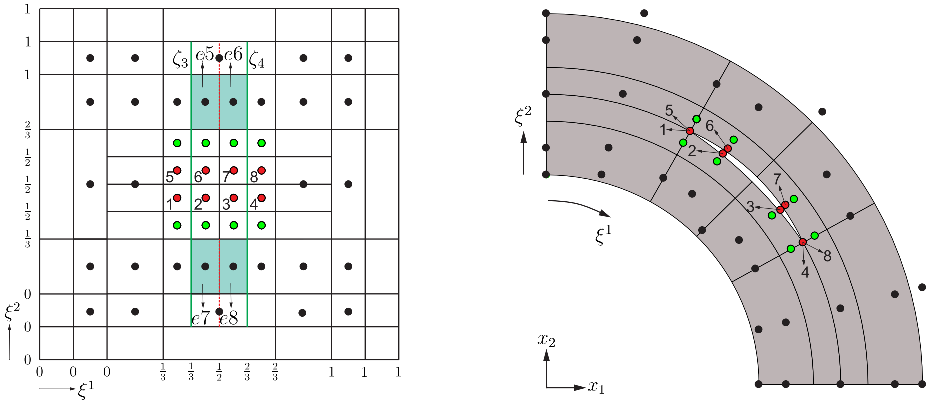

(a) Ω in the parameter domain (b) Ω in the physical domain

Figure 5. Example of inserting a crack with control points at the crack tip.

insertion. To achieve this, we need control points 1, 4, 5 and 8 to be at the crack tip, see Figure 5b. It allows us to parameterise a crack with a minimum number of control points (basis functions) [19]. This is achieved by extending $\mathcal{C}^0$ lines ζ_1 and ζ_2 in Figure 4a one cell further than $\mathcal{C}^0$ lines ζ_3 and ζ_4 in Figure 5a.

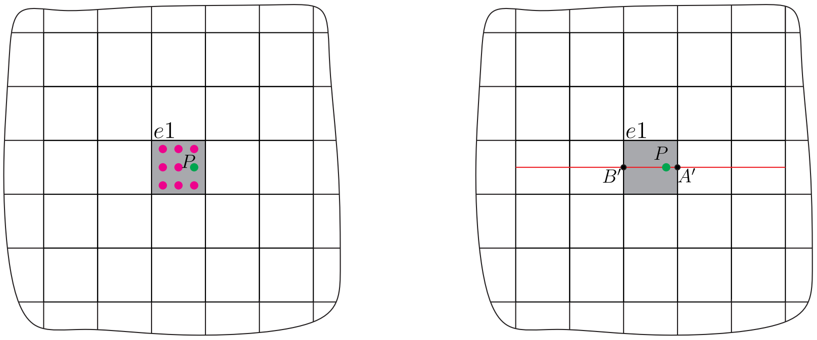

(a) initila geometry Ω (b) Ω with crack before reparameterisation

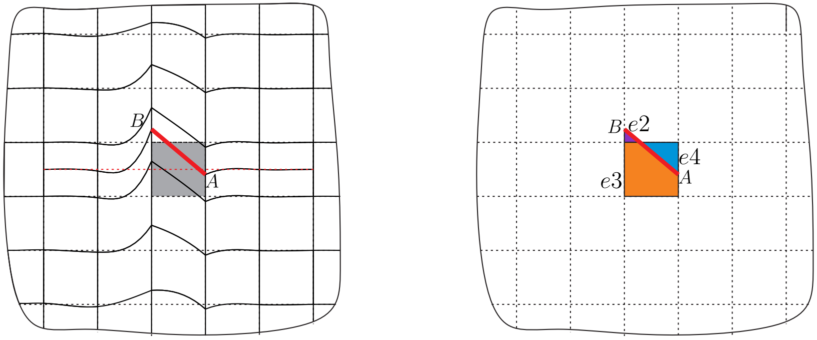

(c) Ω with crack after reparameterisation (d) Ω with crack in a standard finite element discretisation

Figure 6. Example of inserting a crack in the physical domain. Here, the Beźier elements are indicated by solid lines. Isoparametric lines before (dotted) and after (solid) reparameterisation are shown. The inserted crack path is denoted by the red solid line in (c) and (d).

4.2. Crack representation in the physical domain

In isogeometric analysis the crack path is represented by meshline insertions in the parameter domain, which yields $\mathcal{C}^{-1}$-continuous basis functions. In the parameter domain, the crack path insertions will only produce quadrilateral elements, see Figure 5a, and the element type does not change in the process of crack segment insertions. After meshline insertions in the parameter domain, a discrete crack path results in the physical domain, Figure 6b. We consider the case that in Figure 6a, the stress tensor at Gauss point P in element $e1$ violates the stress criterion. Meshlines are then inserted in the parameter domain to represent the crack path passing P. Consequently, a discontinuity $A'B'$ is inserted in the physical domain, Figure 6b. This discontinuity $A'B'$ is a natural product of meshline insertions in the parameter domain. The real crack path passing P in the physical domain will be determined by the normal vector of the maximum principal stress at P. In the present study, a linear crack path is assumed for the insertion of the initial crack segment (line AB in Figure 6c). In general, the inserted crack path will not coincide with an isoparametric line in the physical domain, see Figure 6c. To enforce this, the solid body Ω is reparameterised, as illustrated by the solid lines in Figure 6c. In the figure, elements are quadrilateral. Note that in a standard finite element method, the crack path insertion would produce a different type of elements, Figure 6d, where the inserted crack path AB passes through the top and right edges of element $e1$. After the insertion of crack path AB, we obtain the quadrilateral element $e3$ (after proper modification) and the triangular elements $e2$ and $e4$. This is inconvenient from an implementation point of view.

DOI: 10.1002/nme

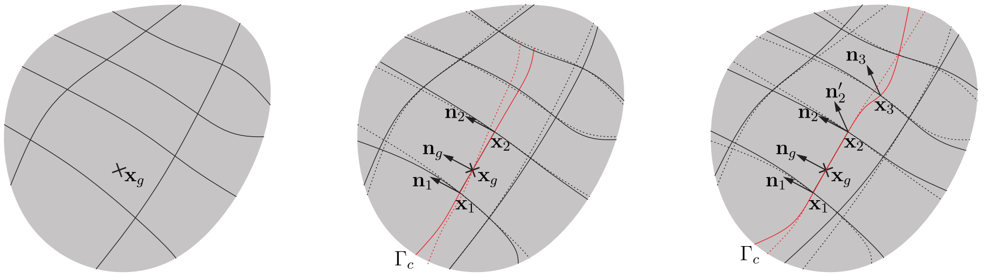

(a) no crack (b) crack nucleation (c) crack propagation

Figure 7. Crack path after crack nucleation and propagation. Isoparametric lines before (dotted) and after (solid) reparameterisation are shown. Red solid curve denotes the crack interface Γ_c.

5. IMPLEMENTATION ASPECTS

In Equations (20) and (22) formulations for crack propagation analysis were introduced without a pre-defined crack interface. Furthermore, the technique has been used to introduce a new crack interface or discontinuity in a solid body, Section 4. In this section, the adaptive refinement for free crack growth is outlined in the context of an isogeometric framework. First, the refinement procedure for crack growth is outlined in detail. Next, the mapping of the displacement vector and the history variables to the mesh will be explained. For the clarity of the presentation, the treatment will be for two dimensions.

5.1. *Adaptive analysis of crack growth*

When the maximum principal stress exceeds the fracture strength t_u at a certain integration point $\mathbf{x}_g$, a crack nucleates and a new crack segment is inserted through the integration point, see Figure 7b. The crack path direction is given by the normal vector $\mathbf{n}_g$ corresponding to the direction of maximum principal stress at $\mathbf{x}_g$. Due to the lack of knowledge about the crack curvature, we assume the initial crack segment after the crack nucleation to be a straight line, i.e. the segment between $\mathbf{x}_1$ and $\mathbf{x}_2$ in Figure 7b. The crack tips $\mathbf{x}_1$ and $\mathbf{x}_2$ are intersections of the linear crack segment with isoparametric lines corresponding to element boundaries (dashed lines in Figure 7b). The normal vectors $\mathbf{n}_1$ and $\mathbf{n}_2$ correspond to the direction of the maximum principal stress at $\mathbf{x}_g$, i.e. $\mathbf{n}_1 = \mathbf{n}_2 = \mathbf{n}_g$. In general, the inserted initial crack segment will not coincide with an isoparametric line in the physical mesh, see Figure 7b. To make the crack segment coincide with an isoparametric line, the solid body Ω is reparameterised. In Figure 7b the isoparametric lines after reparameterisation are denoted by solid lines.

While the use of B-splines and T-splines in isogeometric analysis enforces higher-order continuity, this is lost at the crack tip, and continuity is reduced to $\mathcal{C}^0$. Consequently, the stress tensor at the crack tip is not uniquely defined. An average stress tensor is therefore computed assumed on the basis of stress tensor values close to the crack tip [55]. Typically, the averaged stress tensor is calculated by using a Gaussian weight function:

$$w = \frac{1}{(2\pi)^{\frac{3}{2}} l^3} \exp\left(-\frac{r^2}{2l^2}\right) \tag{26}$$

where w is the weight, l is the smoothing length, which determines how quickly w decays aways from a crack tip and is frequently chosen about three times a typical element size, and r is the distance to the crack tip. The averaged stress tensor is employed to determine the direction of the normal vector at the end point $\mathbf{x}_3$, see Figure 7c.

Crack propagation is determined by the comparison of fracture strength t_u and maximum principal stress σ_1 at all integration points in the elements ahead of the crack tip. If σ_1 exceeds t_u, the crack is propagated. Herein, the crack is extended over one element in the parameter domain, see Figure 7c. The starting position of a new crack segment is at the the tip where the crack

DOI: 10.1002/nme

propagation criterion is violated (here: $\mathbf{x}_2$ and $\mathbf{n}_2$). The normal vector at the end point $\mathbf{x}_3$ matches the principal direction $\mathbf{n}_2'$ of averaged stress tensor at the start point $\mathbf{x}_2$, i.e. $\mathbf{n}_3 = \mathbf{n}_2'$ in Figure 7c. In this study, the normal and corresponding tangent vectors vary linearly from $\mathbf{n}_2$ at $\mathbf{x}_2$ to $\mathbf{n}_3$ at $\mathbf{x}_3$. After insertion of a new crack segment, reparameterisation of the solid body Ω is carried out in order to match the new crack segment with its isoparametric lines. The isoparametric lines before and after reparameterisation are indicated as dotted and solid lines respectively in Figure 7c.

5.2. *Update of the displacement vector and the history variables*

In the process of crack nucleation and propagation, new elements and control points are introduced due to the insertion of new crack segments. In addition, after the insertion of a new crack segment, reparameterisation of the solid body is required to enforce the crack segment and isoparametric lines to coincide. As a result, the LR T-mesh control net is modified. For non-linear problems, this requires a transfer of displacements from previous time step t to provide initial values at time step $t + \Delta t$. In the analysis, we have to consider two types of displacement transfer: (I) transfer due to the insertion of a new crack segment, and (II) transfer due to the reparameterisation of the solid body. We carry out a type (I) transfer and subsequently a type (II) transfer.

For a type (I) transfer, new elements are introduced in the LR T-mesh ${}^{t}\mathcal{T}$, yielding a new LR T-mesh ${}^{t+\Delta t}\mathcal{T}$. The transfer of the displacement vector from old elements to new elements is exact due to the nested finer mesh introduced by the insertion of new crack segments. We consider a state vector ${}^{t}\mathbf{U}$, obtained at time step t. The corresponding LR T-spline space is ${}^{t}\mathcal{N}$. For the next time step $t + \Delta t$, new elements and control points are introduced. We denote the LR T-spline space at time step $t + \Delta t$ by ${}^{t+\Delta t}\mathcal{N}$. In the crack propagation analysis, we need to map the vector ${}^{t}\mathbf{U}$ at time step t to produce a new initial vector ${}_{0}^{t+\Delta t}\mathbf{U}$ at time step $t + \Delta t$,

$$ {}_{0}^{t+\Delta t}\mathbf{U} = (\mathbf{S})^{\mathrm{T}}\, {}^{t}\mathbf{U} \tag{27}$$

where $\mathbf{S}$ denotes the refinement operator between LR T-meshes ${}^{t}\mathcal{T}$ and ${}^{t+\Delta t}\mathcal{T}$, Equation (12). The insertion of a new crack segment also requires the update of history parameters of integration points along Γ_c, which is done similar to the approach in Equation (27).

For a type (II) transfer, we must determine the state vector ${}_{0}^{t+\Delta t}\mathbf{U}_r$ which corresponds to the reparameterised LR T-mesh ${}^{t+\Delta t}\mathcal{T}_r$. Here, ${}^{t+\Delta t}\mathcal{T}_r$ is determined by the reparameterisation of ${}^{t+\Delta t}\mathcal{T}$ upon the insertion of a new crack segment. The corresponding LR T-spline space is ${}^{t+\Delta t}\mathcal{N}_r$. Herein, a global least-squares fit is employed to carry out the mapping of ${}_{0}^{t+\Delta t}\mathbf{U}$ to ${}_{0}^{t+\Delta t}\mathbf{U}_r$, which is achieved by minimising:

$$ \psi = \int_{\Omega} \left\| {}_{0}^{t+\Delta t}\mathbf{u}_r - {}^{t+\Delta t}\mathbf{u} \right\| \mathrm{d}\Omega = \int_{\Omega} \left\| {}^{t+\Delta t}\mathbf{N}_r \; {}_{0}^{t+\Delta t}\mathbf{U}_r - {}^{t+\Delta t}\mathbf{u} \right\| \mathrm{d}\Omega \tag{28}$$

in which $\mathbf{u}$ and $\mathbf{u}_r$ are displacements, and ${}^{t+\Delta t}\mathbf{N}_r$ denotes basis functions associated with the LR T-mesh ${}^{t+\Delta t}\mathcal{T}_r$ at time step $t + \Delta t$. Minimising Equation (28) with respect to ${}_{0}^{t+\Delta t}\mathbf{U}_r$ yields:

$$ \mathbf{M}\; {}_{0}^{t+\Delta t}\mathbf{U}_r = \mathbf{p} \tag{29}$$

with

$$ \mathbf{M} = \int_{\Omega} \left({}^{t+\Delta t}\mathbf{N}_r \right)^{\mathrm{T}}\, {}^{t+\Delta t}\mathbf{N}_r \mathrm{d}\Omega \tag{30}$$

which is obtained directly by Gaussian quadrature at each element on the LR T-mesh ${}^{t+\Delta t}\mathcal{T}_r$ at time step $t + \Delta t$, and

$$ \mathbf{p} = \int_{\Omega} \left({}^{t+\Delta t}\mathbf{N}_r \right)^{\mathrm{T}}\, {}^{t+\Delta t}\mathbf{u} \mathrm{d}\Omega = \int_{\Omega^t} \left({}^{t+\Delta t}\mathbf{N}_r \right)^{\mathrm{T}} \left({}^{t+\Delta t}\mathbf{N} \right) {}^{t+\Delta t}\mathbf{U} \mathrm{d}\Omega \tag{31}$$

where the integration is carried out at each element on the LR T-mesh ${}^{t+\Delta t}\mathcal{T}$ at time step $t + \Delta t$. ${}^{t+\Delta t}\mathbf{N}$ and ${}^{t+\Delta t}\mathbf{N}_r$ represent basis functions associated with the LR T-meshes ${}^{t+\Delta t}\mathcal{T}$ and ${}^{t+\Delta t}\mathcal{T}_r$, respectively.

6. REPARAMETERISATION OF THE LR T-MESH AFTER CRACK INSERTION

After the insertion of a crack segment, the parameterisation of the solid body Ω has changed. In Figure 7, for example, the crack segment is inserted through $\xi^2 = \xi^c$ in the parameter domain. The isoparametric line for $\xi^2 = \xi^c$ is visualised in red. The line moves through Ω after the insertion of a crack segment. Before reparameterisation of the body, the isoparametric line corresponding to $\xi^2 = \xi^c$ (dotted lines in the physical domain) is not aligned with the inserted crack segment (solid lines in the physical domain). Thus, a reparameterisation of the body must be carried out in order to align the isoparametric lines with the inserted crack segment.

6.1. Crack path parameterisation

Herein, a crack is extended per element. For crack nucleation, the fracture criterion is checked at all integration points. Upon violation, an initial crack path is prescribed and inserted through the integration point. In case of crack propagation, the fracture criterion is checked ahead of the crack tip. If it is violated, the crack path is extended over one element in the parameter domain. We will now illustrate the algorithm for the insertion of an initial crack path and the propagation of a crack. We consider a solid body Ω defined by a T-spline mesh to illustrate the concept, see Figure 8.

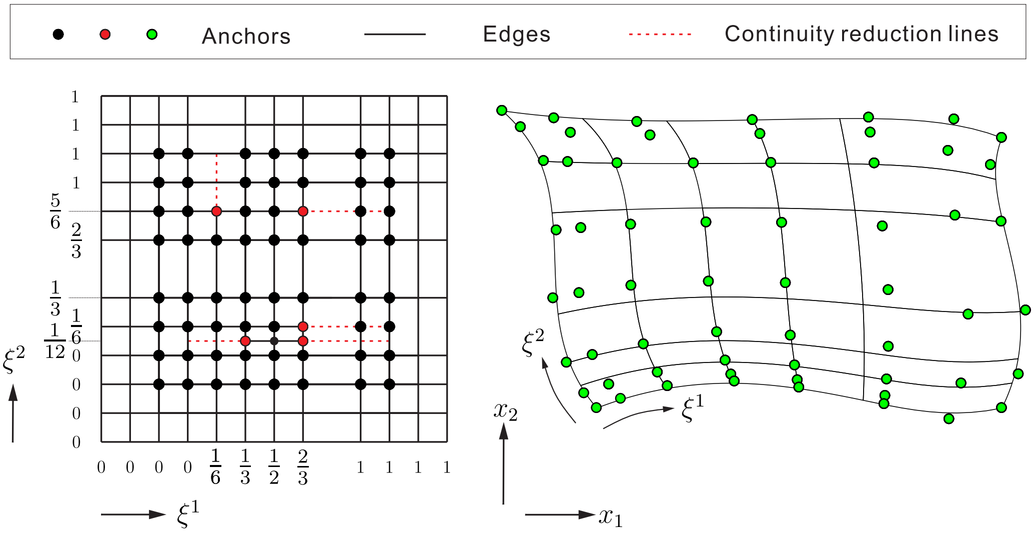

(a) Ω in the parameter domain (b) Ω in the physical domain

Figure 8. Initial geometry of a solid body Ω.

6.1.1. Insertion of an initial crack path For the insertion of the initial crack, we must check the fracture criterion at each Gauss point, Figure 9a, where the Gauss points are indicated by (blue) squares. When the fracture criterion is violated, e.g., at Gauss point G in element e_1, Figure 9a, a crack segment is inserted through this Gauss point. The normal vector $\mathbf{n}_g$, which corresponds to the direction of the maximum principal stress, is employed to set the direction of the initial crack segment. Since there is no information about the curvature of the crack segment, the initial crack path is assumed to be a straight line, see Figure 9b. Generally, a newly inserted crack segment will not coincide with an isoparametric line in the mesh, see the purple and red lines in Figure 9b. Therefore, the solid must be reparamaterised in order to enforce the crack segment and the isoparametric lines coincide. For this purpose, first a discontinuity is inserted which passes through Gauss point G of element e_1 (see also Section 4), Figure 10. Obviously, the crack path does not align with the isoparametric line in Ω, Figure 10b. To enable the alignment of the crack path and the isoparametric lines, the linear crack path must be parameterised. However, the nucleation criterion does not provide information about the length, and the start and end points of the linear crack

DOI: 10.1002/nme

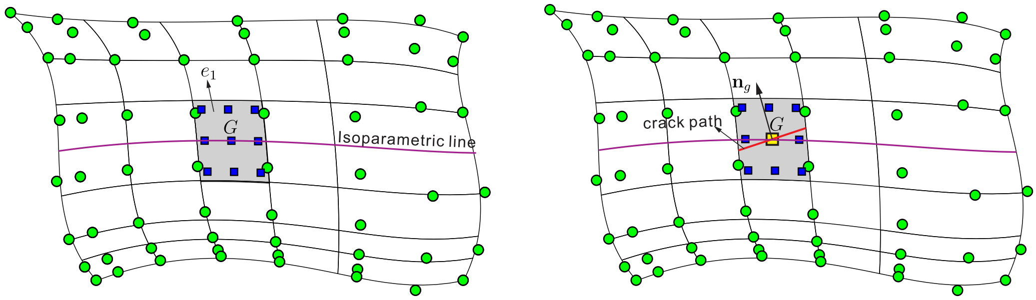

(a) Gauss points in element e_1 and isoparametric lines passing through Gauss point G

(b) insertion of the initial crack

Figure 9. Insertion of an initial crack path passing through Gauss point G in element e_1.

path. We therefore assume that the start and end points are the intersections between the linear crack segment and the isoparametric lines which correspond to the element boundaries (black solid lines in Figure 11). To compute the intersection points A and D, the Bézier control points of the element boundaries [28] must be obtained, denoted by blue diamonds in Figure 11. In this study, cubic T-splines have been used, which produce four Bézier control points per element boundary. We take intersection point D as an example to illustrate the concept. The linear crack segment can be expressed as:

$$ax_1 + bx_2 = c \qquad \Rightarrow \qquad \text{vector form} \qquad \mathbf{Q} \cdot \mathbf{X} = h \tag{32}$$

where $\mathbf{Q} = (a,\, b)^{\mathrm{T}}$ and $\mathbf{X} = (x_1,\, x_2)^{\mathrm{T}}$. Its Bézier form for the element boundary with point D is:

$$\mathbf{X}(t) = (1-t)^3\mathbf{X}_1 + 3t(1-t)^2\mathbf{X}_2 + 3t^2(1-t)\mathbf{X}_3 + t^3\mathbf{X}_4 \qquad t \in [0,\, 1] \tag{33}$$

where $\mathbf{X}_1 \sim \mathbf{X}_4$ are Bézier control points used to define the element boundary, Figure 11. Substitution of Equation (33) into Equation (32) yields the solution for the point D:

$$(1-t)^3\left(\mathbf{Q}\cdot\mathbf{X}_1\right) + 3t(1-t)^2\left(\mathbf{Q}\cdot\mathbf{X}_2\right) + 3t^2(1-t)\left(\mathbf{Q}\cdot\mathbf{X}_3\right) + t^3\left(\mathbf{Q}\cdot\mathbf{X}_4\right) - h = 0 \tag{34}$$

In a general form, Equation (34) can be written as:

$$at^3 + bt^2 + ct + d = 0 \tag{35}$$

where coefficients a, b, c and d are functions of $\mathbf{Q}$ and Bézier control points $\mathbf{X}_1 \sim \mathbf{X}_4$. For its solution, we consider two cases: $a \neq 0$ and $a = 0$, and only real solutions are considered. Substituting the real solutions in Equation (33) provides an intersection point H. If the intersection point H is on the element boundaries defined by the Bézier control points $\mathbf{X}_1 \sim \mathbf{X}_4$, this solution is kept and the intersection point H is the solution for point D, see Figure 11.

Having calculated the intersection points A and D, the linear crack path is defined. To align the linear crack path with the isoparametric line in Ω, the crack path must be parameterised similarly. In element e_1, the isoparametric line is defined as a cubic Bézier curve because of the $\mathcal{C}^0$ lines at the element boundaries, see Figure 10b. Hence the linear crack path must be defined in a cubic Bézier form. The corresponding Bézier control points (Figure 11) are:

$$\mathbf{X}_A = \mathbf{X}_A \qquad \mathbf{X}_B = \frac{(2\mathbf{X}_A + \mathbf{X}_D)}{3} \qquad \mathbf{X}_C = \frac{(\mathbf{X}_A + 2\mathbf{X}_D)}{3} \qquad \mathbf{X}_D = \mathbf{X}_D \tag{36}$$

After determining the Bézier control points $\mathbf{X}_A \sim \mathbf{X}_D$ for the linear crack path, the displacements at the control points between the linear crack segment and the isoparametric line are given as:

$$\mathbf{V}_A = \mathbf{X}_A - \mathbf{X}_{A'} \quad \mathbf{V}_B = \mathbf{X}_B - \mathbf{X}_{B'} \quad \mathbf{V}_C = \mathbf{X}_C - \mathbf{X}_{C'} \quad \mathbf{V}_D = \mathbf{X}_D - \mathbf{X}_{D'} \tag{37}$$

which will be used to determine the control net after the insertion of initial crack path, Figure 12b. The formulation and algorithm of determining the control net will be outlined in Section 6.2.

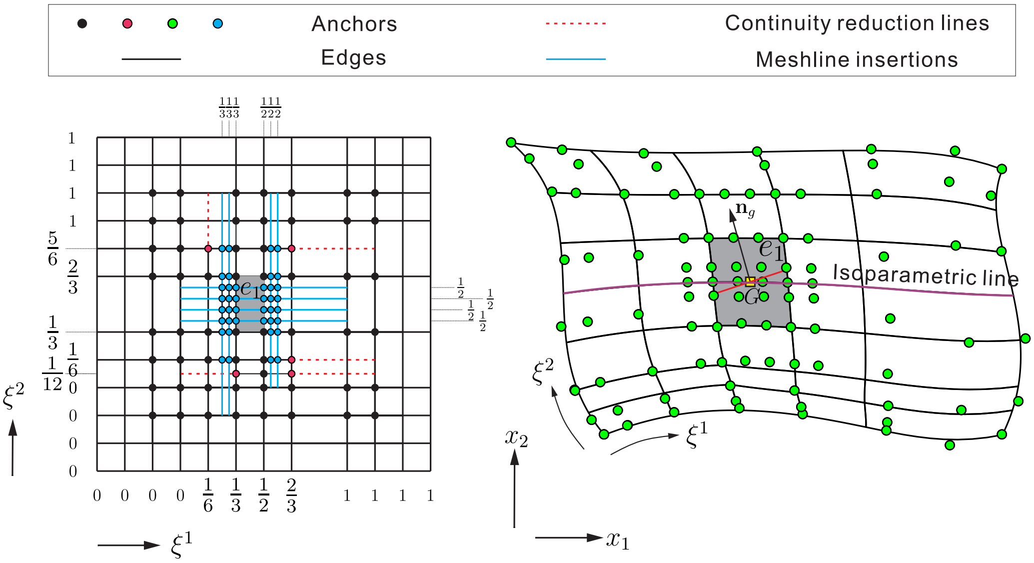

(a) Ω in the parameter domain (b) Ω in the physical domain

Figure 10. Insertion of the initial crack path passing through Gauss point G in element e_1 before reparameterisation. Here, the parameter value ξ^2 of G is $\xi^2 = 0.5$.

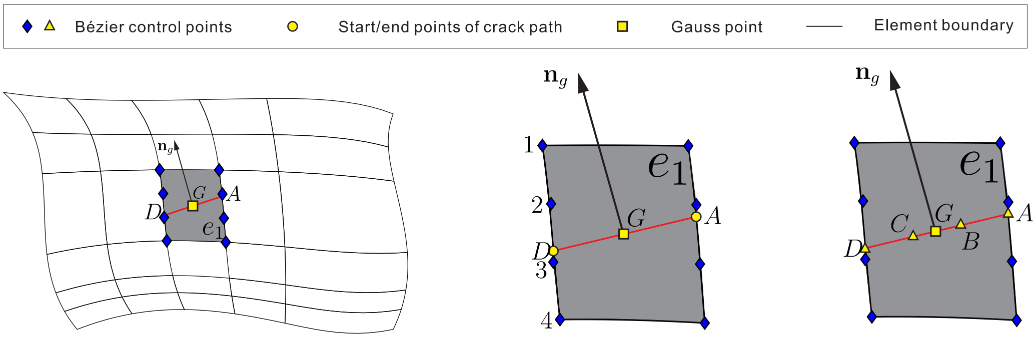

(a) Bézier control points of element e_1 (b) start/end points and Bézier control points of crack path

Figure 11. Definition of the initial crack path. Here, the T-mesh before insertion of the linear crack segment is employed to determine the start/end points of the crack path.

6.1.2. Propagation of the crack path For crack propagation, the stress in front of the crack tip is examined, see points A and D in Figure 13. We now assumed that the fracture criterion is violated at the crack tip at point D. Then, the crack is extended over one element in the parameter domain, as shown in Figure 13a. Due to the $\mathcal{C}^0$ lines at the element boundaries, the previous crack path from A to D will not change after the insertion of a new crack segment, Figure 14c. The starting point of an inserted curved crack path is described by the position and normal vectors of tip D, $\mathbf{X}_D$ and $\mathbf{n}_D$, respectively, see Figure 14. The normal vector at the end point H' should match the principal direction of the average stress tensor at D, see Figures 14b and 14c. We denote the principal direction of the average stress tensor at D by $\mathbf{n}'_D$. Due to the $\mathcal{C}^0$ lines at the element boundaries, the crack path that is inserted between points D and H', Figure 14, is a cubic Bézier curve. The direction tangent to a Bézier curve at its endpoint is parallel to the vector defined by the control polygon $\overline{F'H'}$, Figure 14c. Suppose now that $\mathbf{n}'_D = \{a,\, b\}^{\mathrm{T}}$, then:

$$a\left(x_1^{H'} - x_1^{F'}\right) + b\left(x_2^{H'} - x_2^{F'}\right) = 0 \tag{38}$$

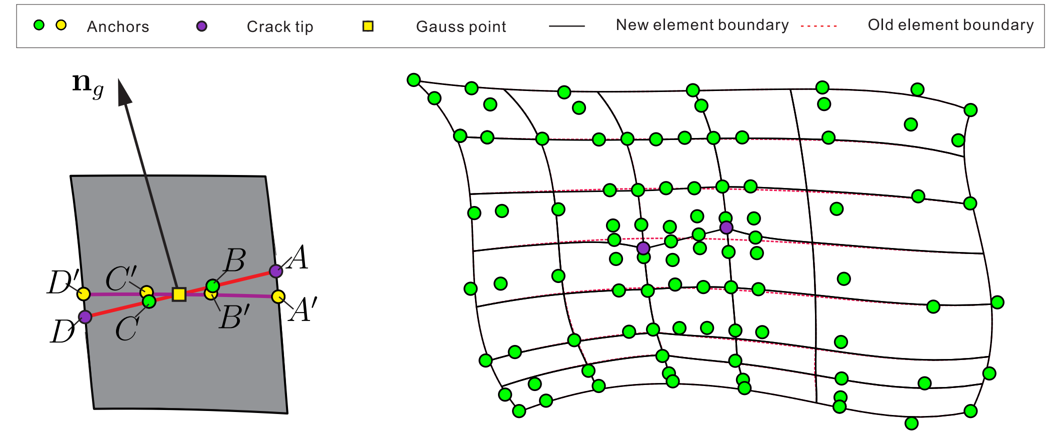

(a) Bézier control point displacement of crack path (b) Ω in the physical domain

Figure 12. Determination of Bézier control point displacement of crack path and the final parameterisation of Ω. Here, Ω in the physical domain before reparameterisation (dashed lines) and after reparameterisation (solid lines) are shown.

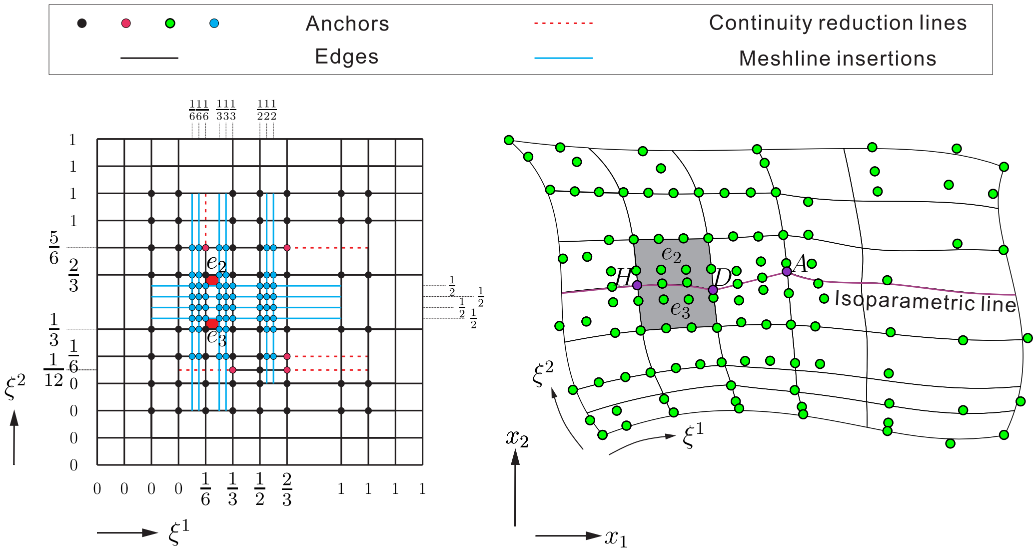

(a) Ω in the parameter domain (b) Ω in the physical domain

Figure 13. Insertion of a new crack path passing through crack tip D before reparameterisation. Here, the parameter value ξ^2 of D is $\xi^2 = 0.5$.

where the control points $\mathbf{X}_{H'}$ and $\mathbf{X}_{F'}$ are defined as $\mathbf{X}_{H'} = \left(x_1^{H'}, x_2^{H'}\right)$ and $\mathbf{X}_{F'} = \left(x_1^{F'}, x_2^{F'}\right)$, respectively.

No information exists for determining the position of the end point H', and neither on the curvature of the crack path. Therefore, it is assumed that the normal and corresponding tangent vector vary linearly from $\mathbf{n}_D$ at D to $\mathbf{n}'_D$ at H', yielding:

$$\mathbf{X}_{H'} - 3\mathbf{X}_{F'} + 3\mathbf{X}_{E'} - \mathbf{X}_D = 0 \tag{39}$$

where $\mathbf{X}_{E'}$ and $\mathbf{X}_D$ are coordinates of the control points $\mathbf{P}_{E'}$ and $\mathbf{P}_D$. Considering that the direction tangent to a Bézier curve at its endpoint is parallel to the vector defined by the control polygon, we can define a continuously differentiable crack at the tip D, see Figure 14c:

$$\frac{\mathbf{X}_C - \mathbf{X}_D}{\|\mathbf{X}_C - \mathbf{X}_D\|} = \frac{\mathbf{X}_D - \mathbf{X}_{E'}}{\|\mathbf{X}_D - \mathbf{X}_E\|} \tag{40}$$

DOI: 10.1002/nme

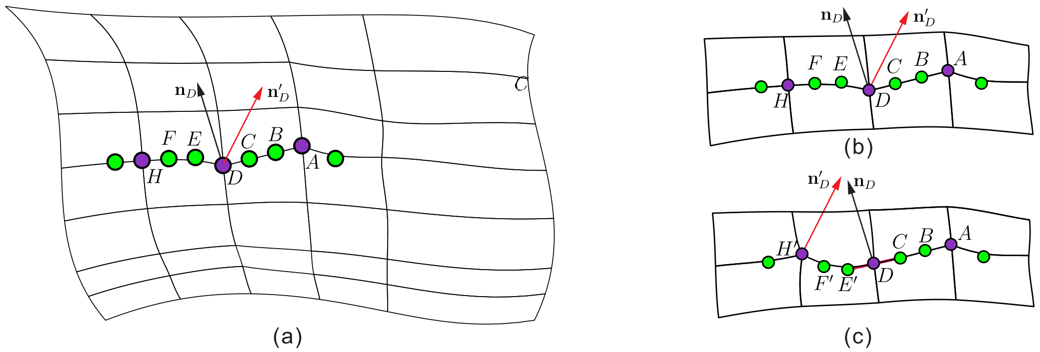

Figure 14. Insertion of a new crack path before reparameterisation and after reparameterisation. (a) solid body Ω with the inserted crack path before reparameterisation; (b) schematic representation of the crack path before reparameterisation; (c) schematic representation of the crack path after reparameterisation.

In this contribution, we restrict the crack to be continuously differentiable cracks. Hence, we assume that the crack is proportionally stretched from the inserted discontinuity (Figure 14b) to the inserted crack path (Figure 14c):

$$\frac{\|\mathbf{X}_{F'}-\mathbf{X}_{H'}\|}{\|\mathbf{X}_F-\mathbf{X}_H\|} = \frac{\|\mathbf{X}_D-\mathbf{X}_{E'}\|}{\|\mathbf{X}_D-\mathbf{X}_E\|} \tag{41}$$

From Equations (38) $\sim$ (41), we obtain the control points $\mathbf{X}_D \sim \mathbf{X}_{H'}$, which are used to compute the displacements of the control points between the crack path and the isoparametric line, see Figure 15a.

$$\mathbf{V}_D = 0 \quad \mathbf{V}'_E = \mathbf{X}'_E - \mathbf{X}_E \quad \mathbf{V}'_F = \mathbf{X}'_F - \mathbf{X}_F \quad \mathbf{V}'_H = \mathbf{X}'_H - \mathbf{X}_H \tag{42}$$

We will employ the results from Equation (42) as Dirichlet boundary conditions to determine the control net after insertion of a crack path, see Figure 15b. For the insertion of the next crack segment, the procedure is the same.

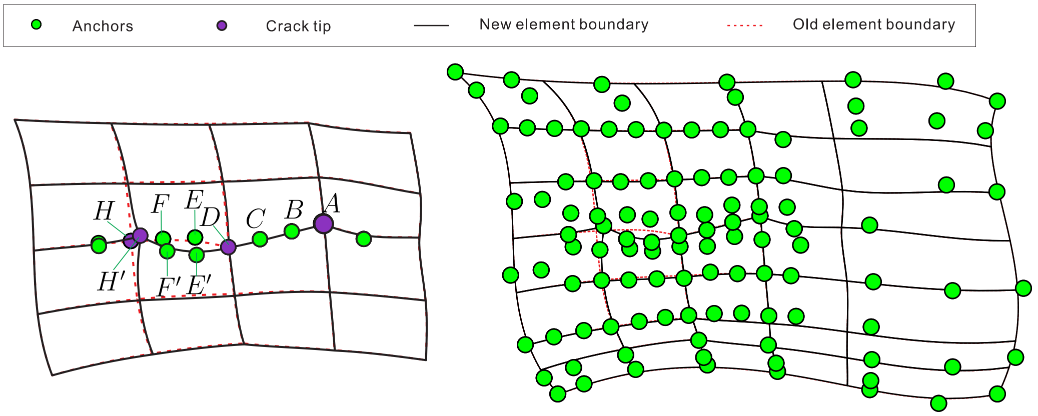

(a) Bézier control point displacement of crack path (b) Ω in the physical domain

Figure 15. Determination of Bézier control point displacement of a crack path and the final parameterisation of Ω. Here, Ω in the physical domain before reparameterisation (dashed lines) and after reparameterisation (solid lines) are shown.

6.2. *Determination of the LR T-mesh control net*

For the analysis of crack propagation, the interior of a solid body changes due to the insertion of a crack path. To align the crack path with the isoparametric lines, the domain must therefore

DOI: 10.1002/nme

be reparameterised. To preserve the exact geometry of the domain, the boundaries of the physical domain, including the cracks, must remain at the same position. In this study, the control net after the insertion of a crack segment has been determined by the requirement that the gradient of the displacement $\mathbf{V}$ is minimised during the parameterisation. $\mathbf{V}$ is the displacement of the physical position $\mathbf{X}'$ with respect to the original position $\mathbf{X}$, $\mathbf{V} = \mathbf{X}' - \mathbf{X} = \{v_1, v_2\}^{\mathrm{T}}$. The displacement field $\mathbf{V}$ is computed by solving one of the two following boundary value problems in the physical domain:

$$\begin{cases} \dfrac{\partial^2 v_1}{\partial x_1^2} = 0 & \mathbf{X} \in \Omega \\ \dfrac{\partial^2 v_2}{\partial x_2^2} = 0 & \mathbf{X} \in \Omega \\ \mathbf{V} = \mathbf{0} & \mathbf{X} \in \partial\Omega \quad \text{and} \quad \mathbf{\Gamma}_c^o \\ \mathbf{V} = \tilde{\mathbf{V}} & \mathbf{X} \in \mathbf{\Gamma}_c^n \end{cases} \tag{43a}$$

$$\begin{cases} \mathbf{LCL}^{\mathrm{T}}\mathbf{V} = \mathbf{0} & \mathbf{X} \in \Omega \\ \mathbf{V} = \mathbf{0} & \mathbf{X} \in \partial\Omega \quad \text{and} \quad \mathbf{\Gamma}_c^o \\ \mathbf{V} = \tilde{\mathbf{V}} & \mathbf{X} \in \mathbf{\Gamma}_c^n \end{cases} \quad \text{with} \quad \mathbf{L} = \begin{bmatrix} \dfrac{\partial}{\partial x_1} & 0 & \dfrac{\partial}{\partial x_2} \\ 0 & \dfrac{\partial}{\partial x_2} & \dfrac{\partial}{\partial x_1} \end{bmatrix} \tag{43b}$$

where $\partial\Omega$ is the boundary of domain Ω, $\mathbf{\Gamma}_c^o$ denotes the inserted crack path, $\mathbf{\Gamma}_c^n$ represents the crack path to be inserted next, $\tilde{\mathbf{V}}$ contains the displacements at the control points, see Equations (37) and (42); and $\mathbf{C}$ is the constitutive matrix of the bulk material.

The boundary value problem of Equation (43a) is uncoupled in the x_1 and x_2 directions. Equation (43b) describes an elastic behaviour on the domain Ω, and is coupled in x_1 and x_2 directions. Both boundary value problems are solved in a standard manner by casting them in a the weak form through multiplication by a test function $\delta\mathbf{V}$ and integration over the domain. LR T-spline basis functions $\mathcal{T}$ are employed to describe the geometry of the domain Ω and to approximate the displacement $\mathbf{V}$. Solution yields the displacement field $\mathbf{V}$, and the new positions of the control points are given by $\mathbf{X}' = \mathbf{X} + \mathbf{V}$, see Figures 12b and 15b.

7. EXAMPLE CALCULATIONS

Two crack propagation problems are now considered. Equation (43a) is employed to solve the domain reparameterisation in the first example (Section 7.1), while Equation (43b) is considered for the second example in Section 7.2. In both cases linear, isotropic elasticity is used for the bulk. Mesh objectivity was verified for both examples. These results, however, are not included to keep the presentation compact and focus on the main findings.

An exponential cohesive law is employed to describe cohesive fracture [56] in mode-I:

$$t_n = t_u \exp\left(-\frac{t_u}{\mathcal{G}_c}\kappa\right) \tag{44}$$

while the shear fracture resistance is neglected. The history parameter κ is determined by the loading function $f = [\![v_n]\!] - \kappa$ [19]. For unloading, a secant stiffness is used. To avoid interpenetration, a penalty stiffness $k_p = 1 \times 10^5$ MPa/mm is specified in the normal direction.

7.1. L-shaped beam peeling test

An L-shaped concrete panel is considered, which is subjected to a vertical concentrated load, see Figure 16 [57], and simulations of crack propagation using extended finite elements were reported in [58]. The Young's modulus $E = 20$ GPa and the Poisson's ratio $\nu = 0.18$. Plane-stress

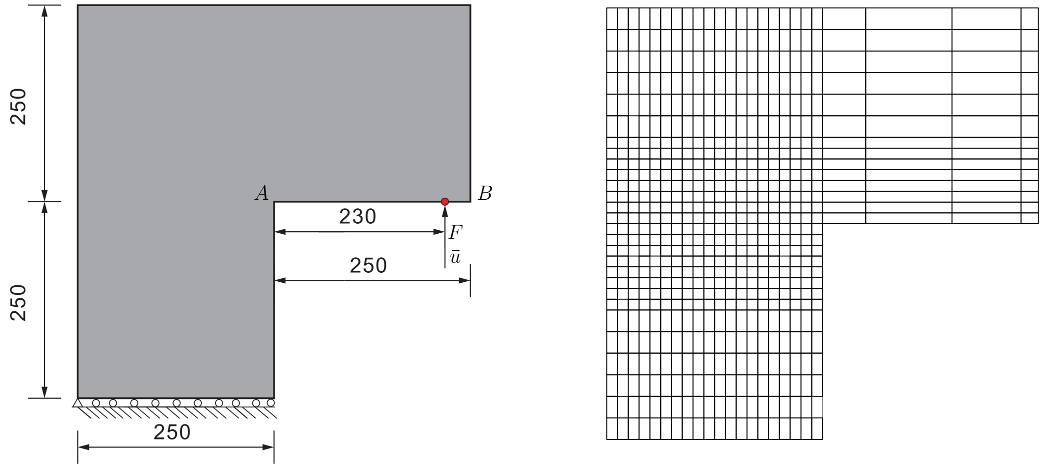

(a) geometry (in mm) and boundary conditions

(b) Bézier element discretisation of the beam

Figure 16. L-shaped beam subjected to a vertical load.

conditions are assumed. The tensile strength and fracture energy are given by $t_u = 2.5$ MPa and $\mathcal{G}_c = 0.13$ N/mm, respectively. Displacement control has been adopted to fully track the load-displacement path with steps of 0.01 mm. The initial discretisation of the beam was using linear NURBS with a knot vector $\left(\Xi_1^0,\, \Xi_2^0\right) = ([0\ 0\ 1\ 1]\,, [0\ 0\ 1\ 1])$, control points $(0,0)$, $(0,500)$, $(500,0)$ and $(500,500)$, and uniform weight factors $w = 1$. Next, the polynomial degree is increased by order elevation to $p, q = 3$, and knot insertions are carried out for the knot vectors Ξ_1^0 and Ξ_2^0 to generate the new knot vectors

$$\begin{aligned}
\Xi_1 = \Big[&0\ 0\ 0\ 0\ \tfrac{1}{40}\ \tfrac{1}{20}\ \tfrac{3}{40}\ \tfrac{1}{10}\ \tfrac{1}{8}\ \tfrac{3}{20}\ \tfrac{7}{40}\ \tfrac{1}{5}\ \tfrac{9}{40}\ \tfrac{1}{4}\ \tfrac{11}{40}\ \tfrac{3}{10}\\
&\tfrac{13}{40}\ \tfrac{7}{20}\ \tfrac{3}{8}\ \tfrac{2}{5}\ \tfrac{17}{40}\ \tfrac{9}{20}\ \tfrac{19}{40}\ \tfrac{1}{2}\ \tfrac{1}{2}\ \tfrac{1}{2}\ \tfrac{3}{5}\ \tfrac{4}{5}\ \tfrac{24}{25}\ \tfrac{24}{25}\ \tfrac{24}{25}\ 1\ 1\ 1\ 1\Big]\\
\Xi_2 = \Big[&0\ 0\ 0\ 0\ \tfrac{1}{20}\ \tfrac{1}{10}\ \tfrac{3}{20}\ \tfrac{1}{5}\ \tfrac{1}{4}\ \tfrac{3}{10}\ \tfrac{13}{40}\ \tfrac{7}{20}\ \tfrac{3}{8}\ \tfrac{2}{5}\ \tfrac{17}{40}\ \tfrac{9}{20}\ \tfrac{19}{40}\\
&\tfrac{1}{2}\ \tfrac{1}{2}\ \tfrac{1}{2}\ \tfrac{21}{40}\ \tfrac{11}{20}\ \tfrac{23}{40}\ \tfrac{3}{5}\ \tfrac{5}{8}\ \tfrac{7}{10}\ \tfrac{3}{4}\ \tfrac{4}{5}\ \tfrac{17}{20}\ \tfrac{9}{10}\ \tfrac{19}{20}\ 1\ 1\ 1\ 1\Big]
\end{aligned} \tag{45}$$

and the control points $\mathbf{P}$. After the knot insertions, we obtain a rectangular plate. To represent the L-shaped domain, we exclude the influence from the right bottom area in the computation of the stiffness matrix $\mathbf{K}$, see Figure 16b. To represent the traction-free surface along the edge AB in Figure 16b, meshline insertions are performed along AB in the parameter domain, which yields an LR T-spline solution space for the problem.

The load-displacement curve is shown in Figure 17a. A good agreement is obtained with experimental results [57]. Figure 17b shows that also the computed crack path is well within the experimentally observed range [57]. Figure 18 gives contour plots of the principal stress σ_1 for two load levels. The displacement and the stress are smooth due to the $\mathcal{C}^2$-continuity of the cubic LR T-spline basis functions. The crack propagates smoothly through the interface Γ_c and no stress oscillations are observed. The effect of the reparamaterisations on the mesh in the physical domain is clearly observed.

7.2. *SEN beam under four-point shear load*

We next consider a Single-Edge Notched (SEN) concrete beam subjected to anti-symmetric four-point shear loads, see Figure 19a. The shear test was first analysed in [59] and involves a curved crack, which nucleates at the notch and propagates to the upper support. The SEN beam has been

DOI: 10.1002/nme

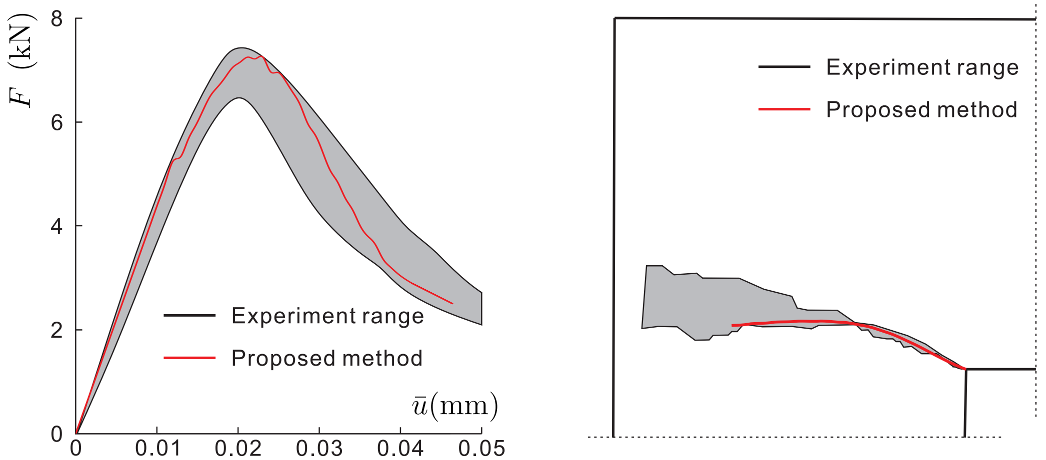

(a) load displacement curve

(b) predicted crack path

Figure 17. Load-displacement response and predicted crack path.

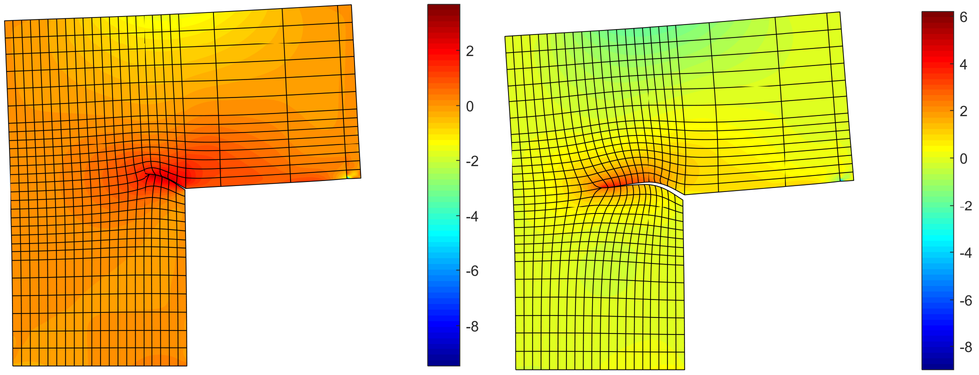

(a) σ_1 contour plot for $\bar{u} = 0.24$mm

(b) σ_1 contour plot for $\bar{u} = 0.43$mm

Figure 18. Stress distribution for different load steps. The displacements have been amplified by a factor 100.

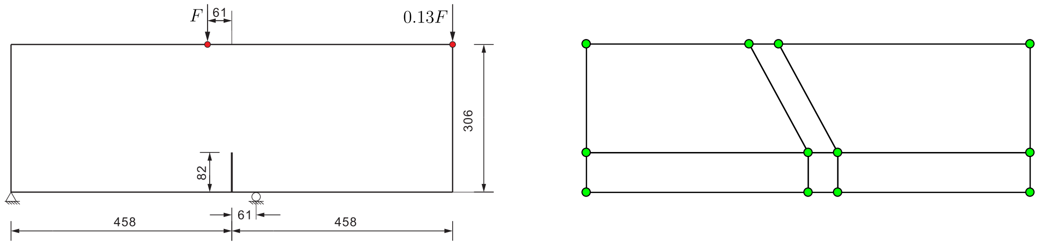

(a) geometry (in mm) and boundary conditions

(b) initial Bézier element discretisation

Figure 19. Single Edge Notched (SEN) beam test.

analysed by many other investigators [10, 60–63]. The material properties of concrete reported in [62] have been used for the simulation: Young's modulus $E = 24.8$ GPa, Poisson's ratio $\nu = 0.18$, tensile strength $t_u = 3.0$ MPa and fracture energy $\mathcal{G}_c = 0.15$ N/mm. The thickness of the specimen is 152 mm. Plane stress conditions have been assumed.

The beam has initially been discretised using linear NURBS with control points $(0, 0)$, $(458, 0)$, $(519, 0)$, $(916, 0)$, $(0, 82)$, $(458, 82)$, $(519, 82)$, $(916, 82)$, $(0, 306)$, $(336, 306)$, $(397, 306)$ and $(916, 306)$, see Figure 19b. The corresponding knot vectors are $\left(\Xi_1^0, \Xi_2^0\right) =$

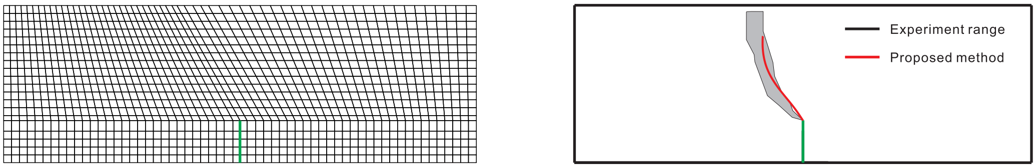

(a) Bézier element discretisation of the beam (b) predicted crack path

Figure 20. Bézier element discretisation and predicted crack path.

$\left(\left[0\ 0\ 0.5\ \frac{519}{916}\ 1\ 1\right],[0\ 0\ 0.5\ 1\ 1]\right)$, and uniform weight factors $w = 1$ have been used initially. Next, order elevation is used to increase the polynomial degree to $p, q = 3$, and knot insertion is employed to introduce more elements in the physical domain, see Figure 20a. The initial, traction-free notch (green line in Figure 20a) is enforced by meshline insertions.

To properly capture the post-peak regime, an arc-length method has been employed [60], in which the Crack Mouth Sliding Displacement (CMSD) has been taken as control parameter. Line searches have been used to improve the convergence behaviour of the Newton-Raphson iterative nonlinear solver [64, 65]. When employing line searches within the arc-length method, we consider the following changes in the standard arc-length method:

$$\mathbf{U}_{i+1}^{j} = \mathbf{U}_i + \eta_{i+1}^{j}\left(\delta\mathbf{U}_{i+1}^{\mathrm{I}} + \delta\lambda_{i+1}^{j}\delta\mathbf{U}_{i+1}^{\mathrm{II}}\right) \tag{46}$$

where i is the iteration number in the arc-length method, j is the iteration number in the line search method, $\mathbf{U}$ is the displacement vector, and $\delta\mathbf{U}$ represents the incremental displacement vector:

$$\delta\mathbf{U}_{i+1}^{\mathrm{I}} = \mathbf{K}_i^{-1}\left(\lambda_{i+1}^{j-1}\mathbf{F}_s - \mathbf{F}_{\mathrm{int},i+1}^{j-1}\right) \qquad \delta\mathbf{U}_{i+1}^{\mathrm{II}} = \mathbf{K}_i^{-1}\mathbf{F}_s \tag{47}$$

with $\mathbf{F}_s$ denoting a normalised load vector, and $\mathbf{K}$ is the stiffness matrix. In Equation (46), η denotes the line search scale factor, $\delta\lambda$ is the load increment factor in the arc-length method, which is obtained as

$$\delta\lambda_{i+1}^{j} = -\frac{\delta U_{i+1,1}^{\mathrm{I},s} - \delta U_{i+1,2}^{\mathrm{I},s}}{\delta U_{i+1,1}^{\mathrm{II},s} - \delta U_{i+1,2}^{\mathrm{II},s}} \quad \text{and} \quad \lambda_{i+1}^{j} = \lambda_{i+1}^{j-1} + \eta_{i+1}^{j}\delta\lambda_{i+1}^{j} \tag{48}$$

where $\delta U_{i+1,1}^{\mathrm{I},s}$ is the sliding displacement component in $\delta\mathbf{U}_{i+1}^{\mathrm{I}}$, and 1 and 2 are the control point indices at the crack mouth.

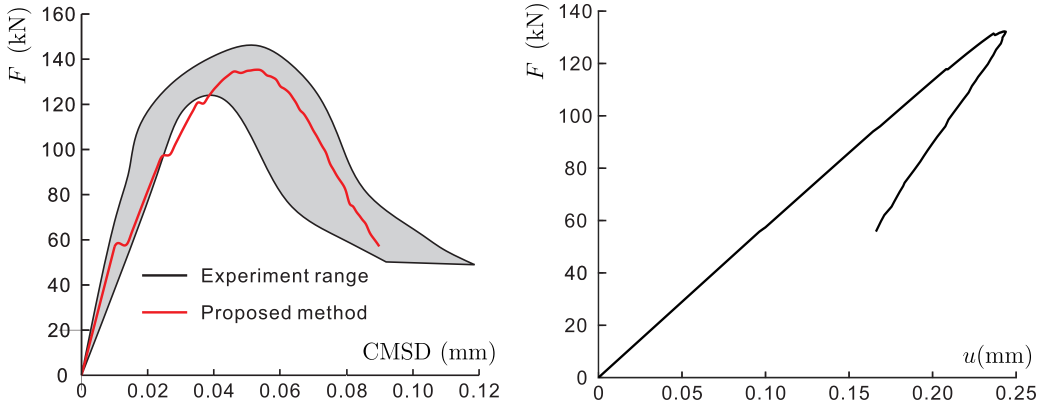

(a) load-CMSD curve (b) load-displacement curve at the top middle loading point

Figure 21. Force-displacement curves for the SEN beam.

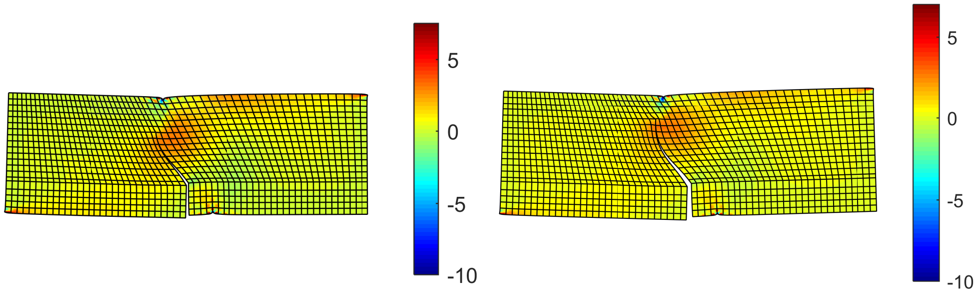

(a) σ_1 contour plot for CMSD $= 0.071$mm (b) σ_1 contour plot for CMSD $= 0.083$mm

Figure 22. Stress distribution for different load steps. The displacements have been amplified by a factor 100.

The response curve is given in terms of the load *vs* CMSD, and as the load *vs* the displacement at the top middle loading point, see Figure 21. The results agree well with the experimental results [59]. The stress contours for different load levels is shown in Figure 22. The crack propagates gradually with the increase of the CMSD. Like for the L-shaped specimen the effect of the reparamaterisation on the mesh in the physical domain is clearly visible upon crack propagation. A comparison of the computed crack path and the experimental results (shaded in gray) is given in Figure 20b. The numerical result agrees well with the experimental observations. The snap-back behaviour in the load-displacement curves at the top middle loading point is also consistent with results in the literature [60, 62, 63].

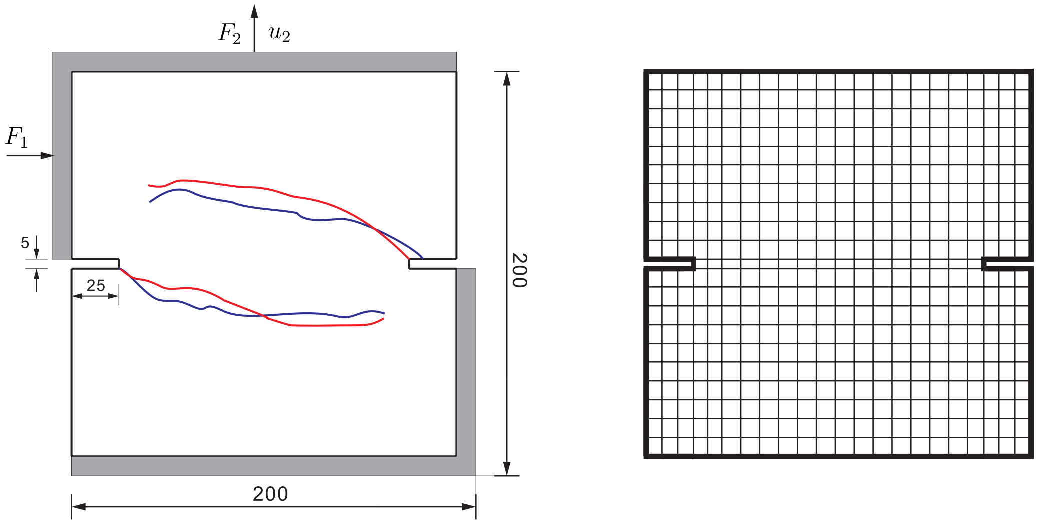

(a) geometry (in mm) and boundary conditions (b) Bézier element discretisation of the beam

Figure 23. Double-Edge-Notched (DEN) tension-shear test. The solid lines in (a) represent crack paths obtained in one of the experiments.

8. LIMITATIONS AND DISCUSSION

The adaptivity and enhanced flexibility that is introduced by Locally Refined T-splines is highly beneficial for the discrete simulation of crack propagation in isogeometric analysis compared to the use of NURBS and even T-splines. While NURBS can only be used along predefined paths or physical interfaces, a freely propagating (cohesive) crack necessitates the use of T-splines as a propagating discrete crack necessarily breaks the tensor-product structure of a NURBS mesh [19].

Nevertheless, care has to be taken because the initial mesh lay-out has to be such that T-junctions can be made throughout the entire propagation of the discrete crack. Local adaptivity, enabled by the use of Locally Refined T-splines, obviates this drawback.

Yet, also LR T-splines have some limitations, and we will illustrate them at the hand of a tension-shear test [66]. Figure 23a shows a Double-Edge Notched (DEN) beam test geometry and boundary conditions. The specimen is first subjected to a prescribed horizontal displacement u_1 until a certain level of the shear force F_1. Subsequently, a vertical load F_2 was applied on the top edge, while keeping F_1 constant.

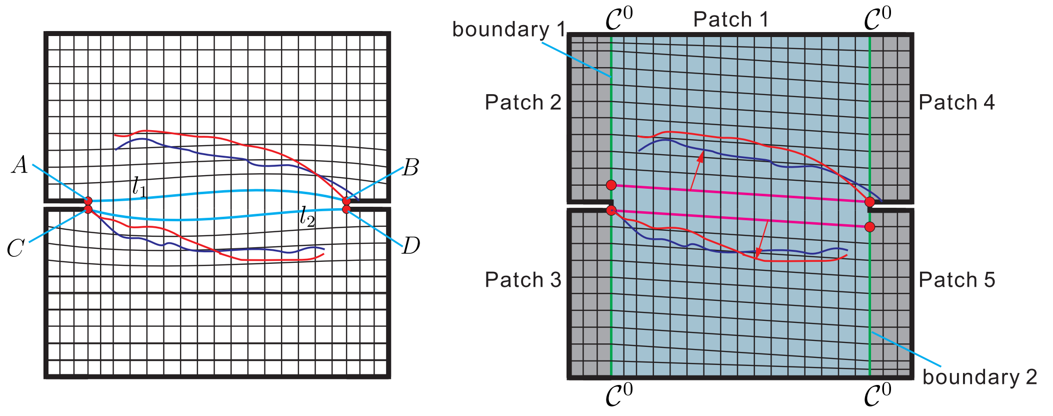

(a) possible crack path for the discretisation in Figure 23b (b) possible Bézier element discretisation

Figure 24. Predicted crack paths for different Bézier element discretisations. Here, the blue lines in (a) and purple lines in (b) are isoparametric lines, which should be aligned with the crack path in the process of crack propagation.

To discretise the domain, we can, in principle, employ a single patch defined by the T-mesh of Figure 23b [19], which shows the Bézier element discretisation. For this mesh, the possible crack paths will be restricted due to the fixed position of the control points A, B, C and D (Figure 24a). Indeed, the cracks will nucleate at the control points B and C. For that, a discontinuity should be inserted through B and C in the parameter domain and hence, in the physical domain. The crack will subsequently propagate and extend per element. To replicate the crack path, we must insert a discontinuity in the parameter domain, so that the crack is presented in the physical domain. For this, the isoparametric lines l_1 and l_2 must be lifted, see Figure 24a. This is, however, not possible because the control points A and D cannot be moved since the geometry of the specimen must be preserved.

Another possibility would be to divide the domain into five patches, see Figure 24b. In this figure, there are four $\mathcal{C}^0$ lines along the boundaries of different patches. Moreover, patch 1 is discretised with inclined lines in order to align the initial mesh with the crack path, see Figure 24b. The disadvantage of this discretisation is that during crack propagation, it is difficult to maintain conforming meshes due to the reparameterisation, see the boundaries 1 and 2 in Figure 24b.

9. CONCLUDING REMARKS

The use of splines as basis functions instead of Lagrange polynomials in finite element analysis has advantages, for instance when it comes to the higher continuity that spline functions bring along. This property can be exploited advantageously when discretising higher-order differential equations, which are usually difficult to solve in an elegant and robust manner when using traditional finite element methods. But it has also advantages for low-order differential equations, since derived quantities like stresses no longer become $\mathcal{C}^{-1}$-continuous at 'element' boundaries, which vastly improves the accuracy of their computation. In particular the use of B-splines and NURBS in isogeometric analysis is very convenient, since they allow for an easy way to increase the order of continuity, also in a two and three-dimensional context.

Likewise, the decrease of the order of continuity can be achieved easily, in the parameter space, which is elegant and avoids full remeshing strategies as in finite elements when cracks and other discontinuities have to be simulated. Particularly for cracks that propagate along a predefined interface, the procedure is straightforward, since the tensor-product structure, which characterises two and three-dimensional formulations of B-splines and NURBS, does not have to be disturbed. This is different for propagating cracks for which the crack path is not predefined. Then, spline technologies which break the tensor-product structure of NURBS must be utilised, like T-splines [19].

Nevertheless, care must also be taken in the latter case, since the use of T-splines implies that it is possible to form T-junctions. When the crack path is such that the initial T-mesh does not allow for this, further propagation cannot be simulated. We have shown that adaptivity, enabled by Locally Refined T-splines (LR T-splines) alleviates this issue. LR T-spline basis functions can represent a crack discontinuity by meshline insertions until C^{-1}-continuity is attained. The technology has been described in detail, including algorithmic and implementation aspects for crack segment insertions and reparameterisation of the domain after crack insertions. Two benchmark cases from the literature demonstrate the dynamic refinement ability of LR T-splines to be suitable for the analysis of discrete crack propagation.

Since a new crack segment is first inserted in the parameter domain and then reparameterised in the physical domain, the initial T-mesh should still be sufficiently aligned with the final crack path. Otherwise, the insertion of a crack segment can be restricted due to the nearness of a domain boundary. The example of a Double-Edge Notched Specimen (DEN) has been used to demonstrate the limitations. Remeshing in the physical domain is an alternative approach to achieve alignment between the initial T-mesh and the final crack path, as is the use of Powell-Sabin B-splines, which are based on triangles, and for which standard remeshing strategies in the physical domain can be used [23, 67].

ACKNOWLEDGEMENT

Financial support from the European Research Council (Advanced Grant 664734 ”PoroFrac”) is gratefully acknowledged.

REFERENCES

[1] Ngo D, Scordelis AC. Finite element analysis of reinforced concrete beams. *Journal of the American Concrete Institute* 1967; **64**:152–163.

[2] Ingraffea AR, Saouma V. Numerical modelling of discrete crack propagation in reinforced and plain concrete. *Fracture Mechanics of Concrete*. Martinus Nijhoff Publishers: Dordrecht, 1985; 171–225.

[3] Camacho GT, Ortiz M. Computational modelling of impact damage in brittle materials. *International Journal of Solids and Structures* 1996; **33**:2899–2938.

[4] Secchi S, Simoni L, Schrefler BA. Mesh adaptation and transfer schemes for discrete fracture propagation in porous materials. *International Journal for Numerical and Analytical Methods in Geomechanics* 2007; **31**:331–345.

[5] Schellekens JCJ, de Borst R. On the numerical integration of interface elements. *International Journal for Numerical Methods in Engineering* 1993; **36**:43–66.

[6] Allix O, Ladevèze P. Interlaminar interface modelling for the prediction of delamination. *Composite Structures* 1992; **22**:235–242.

[7] Schellekens JCJ, de Borst R. Free edge delamination in carbon-epoxy laminates: a novel numerical/experimental approach. *Composite Structures* 1994; **28**:357–373.

[8] Allix O, Corigliano A. Geometrical and interfacial non-lineararities in the analysis of delamination in composites. *International Journal of Solids and Structures* 1999; **36**:2189–2216.

[9] Balzani C, Wagner W. An interface element for the simulation of delamination in unidirectional fiber-reinforced composite laminates. *Engineering Fracture Mechanics* 2008; **75**:2597–2615.

[10] Rots JG. Smeared and discrete representations of localized fracture. *International Journal of Fracture* 1991; **51**:45–59.

[11] de Borst R. Numerical aspects of cohesive-zone models. *Engineering Fracture Mechanics* 2003; **70**:1743–1757.

[12] Xie D, Biggers SB. Progressive crack growth analysis using interface element based on the virtual crack closure technique. *Finite Elements in Analysis and Design* 2006; **42**:977–984.

[13] Xu XP, Needleman A. Numerical simulations of fast crack growth in brittle solids. *Journal of the Mechanics and Physics of Solids* 1994; **42**:1397–1434.

[14] Belytschko T, Black T. Elastic crack growth in finite elements with minimal remeshing. *International Journal for Numerical Methods in Engineering* 1999; **45**:601–620.

[15] Moës N, Dolbow J, Belytschko T. A finite element method for crack growth without remeshing. *International Journal for Numerical Methods in Engineering* 1999; **46**:131–150.

[16] Fries TP, Belytschko T. The extended/generalized finite element method: An overview of the method and its applications. *International Journal for Numerical Methods in Engineering* 2010; **84**:253–304.

[17] de Borst R, Crisfield MA, Remmers JJC, Verhoosel CV. *Non-Linear Finite Element Analysis of Solids and Structures*. second edn., Wiley & Sons: Chichester, 2012.

[18] Khoei A. *Extended Finite Element Method: Theory and Applications*. Wiley & Sons: Chichester, 2014.

[19] Verhoosel CV, Scott MA, de Borst R, Hughes TJR. An isogeometric approach to cohesive zone modeling. *International Journal for Numerical Methods in Engineering* 2011; **87**:336–360.

[20] Irzal F, Remmers JJC, Verhoosel CV, de Borst R. An isogeometric analysis Bézier interface element for mechanical and poromechanical fracture problems. *International Journal for Numerical Methods in Engineering* 2014; **97**:608–628.

[21] Vignollet J, May S, de Borst R. On the numerical integration of isogeometric interface elements. *International Journal for Numerical Methods in Engineering* 2015; **102**:1773–1749.

[22] Vignollet J, May S, de Borst R. Isogeometric analysis of fluid-saturated porous media including flow in the cracks. *International Journal for Numerical Methods in Engineering* 2016; **108**:990–1006.

[23] May S, de Borst R, Vignollet J. Powell-Sabin B-splines for smeared and discrete approaches to fracture in quasi-brittle materials. *Computer Methods in Applied Mechanics and Engineering* 2016; **307**:193–214.

[24] Chen L, Lingen FJ, de Borst R. Adaptive hierarchical refinement of nurbs in cohesive fracture analysis. *International Journal for Numerical Methods in Engineering* 2017; **112**:2151–2173.

[25] de Borst R. *Computational Methods for Fracture in Porous Media: Isogeometric and Extended Finite Element Methods*. Elsevier, 2017.

[26] de Luycker E, Benson DJ, Belytschko T, Bazilevs Y, Hsu MC. X-FEM in isogeometric analysis for linear elastic fracture mechanics. *International Journal for Numerical Methods in Engineering* 2011; **87**:541–565.

[27] Bazilevs Y, Calo VM, Cottrell JA, Evans JA, Hughes TJR, Lipton S, Scott MA, Sederberg TW. Isogeometric analysis using T-splines. *Computer Methods in Applied Mechanics and Engineering* 2010; **199**:229–263.

[28] Scott MA, Borden MJ, Verhoosel CV, Sederberg TW, Hughes TJR. Isogeometric finite element data structures based on Bézier extraction of T-splines. *International Journal for Numerical Methods in Engineering* 2011; **88**:126–156.

[29] Li X, Zheng J, Sederberg TW, Hughes TJR, Scott MA. On linear independence of T-spline blending functions. *Computer Aided Geometric Design* 2012; **29**:63–76.

[30] Morgenstern P, Peterseim D. Analysis-suitable adaptive T-mesh refinement with linear complexity. *Computer Aided Geometric Design* 2015; **34**:50–66.

[31] May S, Vignollet J, de Borst R. The role of the Bézier extraction operator for T-splines of arbitrary degree: linear dependencies, partition of unity property, nesting behaviour and local refinement. *International Journal for Numerical Methods in Engineering* 2015; **103**:547–581.

[32] Chen L, de Borst R. Adaptive refinement of hierarchical t-splines. *Computer Methods in Applied Mechanics and Engineering* 2018; **337**:220–245.

[33] Dörfel MR, Jüttler B, Simeon B. Adaptive isogeometric analysis by local h-refinement with T-splines. *Computer Methods in Applied Mechanics and Engineering* 2010; **199**:264–275.

[34] Scott MA, Li X, Sederberg TW, Hughes TJR. Local refinement of analysis-suitable T-splines. *Computer Methods in Applied Mechanics and Engineering* 2012; **213**:206–222.

[35] Evans EJ, Scott MA, Li X, Thomas DC. Hierarchical T-splines: Analysis-suitability, Bézier extraction, and application as an adaptive basis for isogeometric analysis. *Computer Methods in Applied Mechanics and Engineering* 2015; **284**:1–20.

[36] Hennig P, Kästner M, Morgenstern P, Peterseim D. Adaptive mesh refinement strategies in isogeometric analysis – A computational comparison. *Computer Methods in Applied Mechanics and Engineering* 2017; **316**:424–448.

[37] Wei X, Zhang Y, Liu L, Hughes TJR. Truncated T-splines: Fundamentals and methods. *Computer Methods in Applied Mechanics and Engineering* 2017; **316**:349–372.

[38] de Borst R, Chen L. The role of Bézier extraction in adaptive isogeometric analysis: Local refinement and hierarchical refinement. *International Journal for Numerical Methods in Engineering* 2018; **113**:999–1019.

[39] Chen L, de Borst R. Locally refined T-splines. *International Journal for Numerical Methods in Engineering* 2018; :DOI: 10.1002/nme.5759.

[40] Dokken T, Lyche T, Pettersen KF. Polynomial splines over locally refined box-partitions. *Computer Aided Geometric Design* 2013; **30**:331–356.

[41] Bressan A. Some properties of LR-splines. *Computer Aided Geometric Design* 2013; **30**:778–794.

[42] Johannessen KA, Kvamsdal T, Dokken T. Isogeometric analysis using LR B-splines. *Computer Methods in Applied Mechanics and Engineering* 2014; **269**:471–514.

[43] Johannessen KA, Kumar M, Kvamsdal T. Divergence-conforming discretization for Stokes problem on locally refined meshes using LR B-splines. *Computer Methods in Applied Mechanics and Engineering* 2015; **293**:38–70.

[44] Johannessen KA, Remonato F, Kvamsdal T. On the similarities and differences between classical hierarchical, truncated hierarchical and LR B-splines. *Computer Methods in Applied Mechanics and Engineering* 2015; **291**:64–101.

[45] D S Dugdale DS. Yielding of steel sheets containing slits. *Journal of the Mechanics and Physics of Solids* 1960; **8**:100–104.

[46] Barenblatt GI. The mathematical theory of equilibrium cracks in brittle fracture. *Advances in Applied Mechanics* 1962; **7**:55–129.

[47] Remmers JJC, de Borst R, Needleman A. The simulation of dynamic crack propagation using the cohesive segments method. *Journal of the Mechanics and Physics of Solids* 2008; **56**:70–92.

[48] Chen L, Dornisch W, Klinkel S. Hybrid collocation – Galerkin approach for the analysis of surface represented 3D-solids employing SB-FEM. *Computer Methods in Applied Mechanics and Engineering* 2015; **295**:268–289.

[49] Verhoosel CV, Scott MA, Hughes TJR, de Borst R. An isogeometric analysis approach to gradient damage models. *International Journal for Numerical Methods in Engineering* 2011; **86**:115–134.

[50] Klinkel S, Chen L, Dornisch W. A NURBS based hybrid collocation – Galerkin method for the analysis of boundary represented solids. *Computer Methods in Applied Mechanics and Engineering* 2015; **284**:689–711.

[51] May S, Vignollet J, de Borst R. Powell-Sabin B-splines and unstructured standard T-splines for the solution of Kichhoff-Love plate theory using Bézier extraction. *International Journal for Numerical Methods in Engineering* 2016; **107**:205–233.

[52] Gomez H, Calo VM, Bazilevs Y, Hughes TJR. Isogeometric analysis of the Cahn-Hilliard phase-field model. *Computer Methods in Applied Mechanics and Engineering* 2008; **197**:4333–4352.

[53] Kästner M, Metsch P, de Borst R. Isogeometric analysis of the Cahn–Hilliard equation–a convergence study. *Journal of Computational Physics* 2016; **305**:360–371.

[54] Chen L, Simeon B, Klinkel S. A NURBS based Galerkin approach for the analysis of solids in boundary representation. *Computer Methods in Applied Mechanics and Engineering* 2016; **305**:777–805.

[55] Jirasek M, Zimmermann T. Embedded crack model. part ii: Combination with smeared cracks. *International Journal for Numerical Methods in Engineering* 2001; **50**:1291–1305.

[56] Wells GN, Sluys LJ. A new method for modelling cohesive cracks using finite elements. *International Journal for Numerical Methods in Engineering* 2001; **50**:2667–2682.

[57] Winkler BJ. *Traglastuntersuchungen von unbewehrten und bewehrten Betonstrukturen auf der Grundlage eines objektiven Werkstoffgesetzes für Beton*. Innsbruck University Press, 2001.

[58] Unger JF, Eckardt S, Könke C. Modelling of cohesive crack growth in concrete structures with the extended finite element method. *Computer Methods in Applied Mechanics and Engineering* 2007; **196**:4087–4100.

[59] Ingraffea A, Arrea M. Mixed-mode crack propagation in mortar and concrete. *Technical Report*, Report No. 81 1982.

[60] De Borst R. Computation of post-bifurcation and post-failure behavior of strain-softening solids. *Computers & Structures* 1987; **25**:211–224.

[61] Xie M, Gerstle WH, Rahulkumar P. Energy-based automatic mixed-mode crack-propagation modeling. *Journal of Engineering Mechanics* 1995; **121**:914–923.

[62] Yang Z, Chen J. Fully automatic modelling of cohesive discrete crack propagation in concrete beams using local arc-length methods. *International Journal of Solids and Structures* 2004; **41**:801–826.

[63] Wang Y, Waisman H. From diffuse damage to sharp cohesive cracks: A coupled XFEM framework for failure analysis of quasi-brittle materials. *Computer Methods in Applied Mechanics and Engineering* 2016; **299**:57–89.

[64] Crisfield MA. An arc-length method including line search and acceleration. *International Journal for Numerical Method in Engineering* 1983; **19**:1269–1289.

[65] Schweizerhof KH. Consistent concept for line search algorithms in combination with arc-length constraints. *International Journal for Numerical Methods in Biomedical Engineering* 1993; **9**:773–784.

[66] Nooru-Mohamed MB. Mixed-mode fracture of concrete: an experimental approach. PhD Thesis, Delft University of Technology 1992.

[67] Chen L, de Borst R. Cohesive fracture analysis using Powell-Sabin B-splines. *International Journal for Numerical and Analytical Methods in Geomechanics* 2018; (submitted).